


4-2019

## Electrocatalysis for Proton and Oxygen Reduction Reactions

William Lake

Follow this and additional works at: <https://scholarworks.wm.edu/honorsthesis>

 Part of the [Environmental Chemistry Commons](#), [Inorganic Chemistry Commons](#), [Oil, Gas, and Energy Commons](#), and the [Physical Chemistry Commons](#)

---

### Recommended Citation

Lake, William, "Electrocatalysis for Proton and Oxygen Reduction Reactions" (2019). *Undergraduate Honors Theses*. Paper 1350.

<https://scholarworks.wm.edu/honorsthesis/1350>

This Honors Thesis is brought to you for free and open access by the Theses, Dissertations, & Master Projects at W&M ScholarWorks. It has been accepted for inclusion in Undergraduate Honors Theses by an authorized administrator of W&M ScholarWorks. For more information, please contact [scholarworks@wm.edu](mailto:scholarworks@wm.edu).

# **Electrocatalysis for Proton and Oxygen Reduction Reactions**

A thesis submitted in partial fulfillment of the requirement  
for the degree of Bachelors of Science in Department of Chemistry from  
The College of William and Mary

By  
William R. Lake

Accepted for \_\_\_\_\_

---

**William R. McNamara, Director**

---

**John C. Poutsma**

---

**Nathan M. Kidwell**

---

**Mainak J. Patel**

Williamsburg, VA  
April 29, 2019

## Table of Contents

<b>Acknowledgements</b>	3
<b>List of Figures, Tables, and Schemes</b>	4
<b>List of Appendix Figures</b>	5
<b>Chapter 1: Background</b>	
Global Energy Crisis	8
References	14
<b>Chapter 2: Proton Reduction by Cobalt Schiff-base Complexes</b>	
Introduction	15
Experimental Methods	23
Results and Discussion	27
References	31
Appendix A	32
<b>Chapter 3: Exploration of Catalysts for the Oxygen Reduction Reaction</b>	
Introduction	51
Experimental Methods	57
Results and Discussion	60
References	62
Appendix B	63

## Acknowledgements

I would like to thank Dr. McNamara for his time and effort spent as my research advisor. I learned all I know about chemistry research under his tutelage. I entered his lab without even the most basic knowledge of inorganic chemistry, and he has given me the tools and skills necessary to succeed as a chemist in post-undergraduate life.

I would like to thank Professors J.C. Poutsma, Nathan Kidwell, and Maniak Patel for serving on my honors committee. Professors Poutsma and Kidwell were invaluable in helping me discover the areas of chemistry I am the most fascinated by, and finding ways to marry mathematics and chemistry. Professor Patel was my first applied mathematics professor, and he was eye-opening as to all the places math can take me. Additionally, thank you to my other professors in the Chemistry and Mathematics departments. I deeply enjoyed your classes, and I hope you continue to be as inspiring for other students as you were for me.

Thank you as well to all my coworkers in McNamara lab, especially Ryan DiRisio and Jessica Armstrong, who taught me almost everything I know. Also to Mariah Frank, who with Jessica and Ryan helped with completion of the work in Chapter 2. I'd like also to thank Zach Schiffman and Ankush Joshi for their invaluable help in completion of the work presented in Chapter 3. And thank you to the rest of the McNamara workforce, for making time in lab not only productive but also fulfilling.

Finally, thank you to my family and friends. You have been uplifting and supportive of all of my choices throughout my undergraduate career, and I cannot thank you enough. None of this would have been possible without your grounding presence and love, and I cannot thank you enough.



## List of Figures

Figure 1.1: Global Energy Production	8
Figure 1.2: Tick Populations Spread	9
Figure 2.1: Cyclohexyl Co complex <b>1</b>	15
Figure 2.2: Nitro-substituted Co complexes <b>2,3</b>	15
Figure 2.3: Cyclic Voltammetry experimental setup	16
Figure 2.4: $i_c$ and $i_p$ diagram	16
Figure 2.5: Ideal and non-ideal catalytic waves	18
Figure 2.6: Ideal portion of the wave used in FOWA	19
Figure 2.7: Overpotential Diagram	20
Figure 2.8: Tafel Plot of <b>2</b> at 200 mV/s	22
Figure 2.9: X-Ray Structure of complexes <b>2, 3</b>	27
Figure 2.10: CV of <b>2</b> at 200 mV/s	28
Figure 2.11: CV of <b>3</b> at 200 mV/s	28
Figure 2.12: FOWA linear fit for <b>2</b> and <b>3</b>	29
Figure 3.1: RRDV Diagram	53
Figure 3.2: Structures of tested catalysts for ORR	56
Figure 3.3: RRDV Results for <b>5</b>	60

## List of Tables

Table 1: Electrochemical Analysis Results for <b>2</b> and <b>3</b>	27
---	----

## List of Schemes

Scheme 1.1: Artificial Photosynthesis	11
Scheme 1.2: Hydrogen Fuel Cell	12

Scheme 2.1: Synthesis of <b>2</b> and <b>3</b>	23
--	----

### **List of Equations**

Equations 1-3: Hydrogen Fuel Cell Reactions	12
Equation 4: Proton reduction reaction	15
Equations 5-7: FOWA rate constant determination	17
Equation 8: FOWA slope-rate constant relationship	19
Equation 9: Relating Rate Constants	20
Equation 10: Overpotential Calculation	20
Equations 11-12: TOF and Overpotential Relationship	21
Equations 13-15: Oxygen Reduction Reactions	51
Equation 16: Selectivity of ORR from RRDV	54
Equations 17-19: Overpotential equations for ORR	54

## Appendix Figures

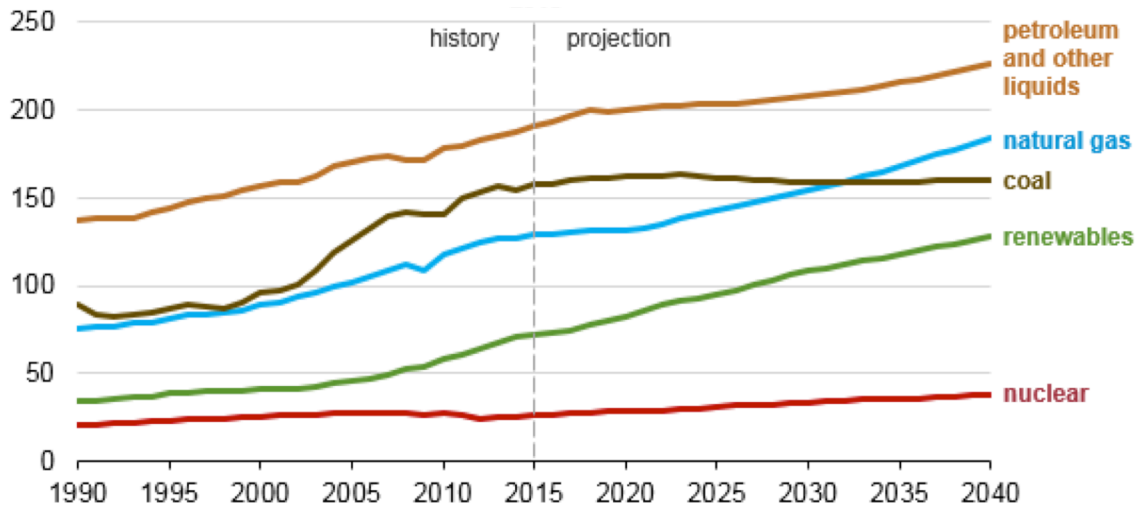
Table A1. Selected bond lengths and angles of <b>2</b> and <b>3</b>	32
Figure A1. Acid Addition Study of <b>2</b> in MeCN at 500 mV/s	33
Figure A2. Acid Addition Study of <b>2</b> in MeCN at 1 V/s	34
Figure A3. Acid Addition Study of <b>3</b> in MeCN at 600 mV/s	35
Figure A4. Acid Addition Study of <b>3</b> in MeCN at 1 mV/s	36
Figure A5-A6. $i_c/i_p$ vs. [TFA] for <b>2</b> and <b>3</b> at $v = 200$ mV/s	37
Figure A7. Background Scan in the region of <b>2</b>	38
Figure A8. Background Scan in the region of <b>3</b>	39
Figure A9. Tafel Plot of <b>2</b> at 200 mV/s	40
Figure A10. Tafel Plot of <b>2</b> at 500 mV/s	41
Figure A11. Tafel Plot of <b>2</b> at 1 V/s	42
Figure A12. Tafel Plot of <b>3</b> at 200 mV/s	43
Figure A13. Tafel Plot of <b>3</b> at 600 mV/s	44
Figure A14. Tafel Plot of <b>3</b> at 1 V/s	45
Figure A15. $k_{cat}$ values at varying scan rates for <b>2</b> and <b>3</b>	46
Figure A16-A17. $^1H$ NMR of <b>2</b> and <b>3</b>	47
Figure A18-A19. HR Mass Spectrum of <b>2</b> and <b>3</b>	48
Figure A20. $k_{obs}$ vs [TFA] for <b>2</b>	49
Figure A20. $k_{obs}$ vs [TFA] for <b>3</b>	50
Figure B1. Acid addition study of <b>1</b> under $O_2$ atmosphere	63
Figure B2. Acid addition study of <b>2</b> under $O_2$ atmosphere	64
Figure B3. Acid addition study of <b>3</b> under $O_2$ atmosphere	65

Figure B4. Acid addition study of <b>4</b> under O <sub>2</sub> atmosphere	66
Figure B5. Acid addition study of <b>5</b> under O <sub>2</sub> atmosphere	67
Figure B6. Acid addition study of <b>6</b> under O <sub>2</sub> atmosphere	68
Figure B7. Acid addition study of <b>7</b> under O <sub>2</sub> atmosphere	69
Figure B8. Acid addition study of <b>8</b> under O <sub>2</sub> atmosphere	70
Figure B9. Acid addition study of <b>9</b> under O <sub>2</sub> atmosphere	71
Figure B10. Acid addition study of <b>10</b> under O <sub>2</sub> atmosphere	72
Figure B11. Catalyst free acid addition study under O <sub>2</sub> atmosphere, Vitreous carbon electrode	73
Figure B12. Catalyst free acid addition study under O <sub>2</sub> atmosphere, Pt electrode	74

## Chapter 1: Introduction

### Background

Today, the global community faces two intrinsically linked problems: growing energy demand and global climate change. Countries like India, Nigeria, and China, outside of the Organization for Economic Cooperation and Development, are dramatically increasing energy use.<sup>1</sup> Their economic growth is the driving factor in rising demand, as they are projected to grow in GDP by 3.8% annually until 2040.<sup>2</sup> In total, world energy consumption is expected to rise by 48% by 2040, from 575 quadrillion BTU in 2015 to 736 quadrillion BTU.<sup>1</sup> Figure 1.1 shows the increase in energy demand, and in particular projects the increased dependence on renewable energy sources.<sup>1</sup>



**Figure 1.1:** Projected world energy consumption, in Btu, by energy source<sup>1</sup>.

The rise in reliance upon renewable energy sources is necessary for future global health, as the three largest energy sources (coal, natural gas, and petroleum) provide energy via combustion of hydrocarbons, which releases greenhouse gasses like carbon dioxide and methane into the world's atmosphere.<sup>3</sup> This increase in greenhouse gas concentration warms the Earth<sup>4</sup>, and the speed of climate change is increasing. From 1990

to 2015, the total warming effect directly attributed to human greenhouse gas emissions increased by 37%.<sup>4</sup> This warming carries with it health risks, energy concerns, and increased incidents of natural disasters like major floods and severe storms.<sup>4</sup> In the US, nine of the top ten single-day floods from 1910 to 2015 occurred after 1990. As shown in figure 1.2, incidents of Lyme disease have doubled since 1991, as the ticks that spread the

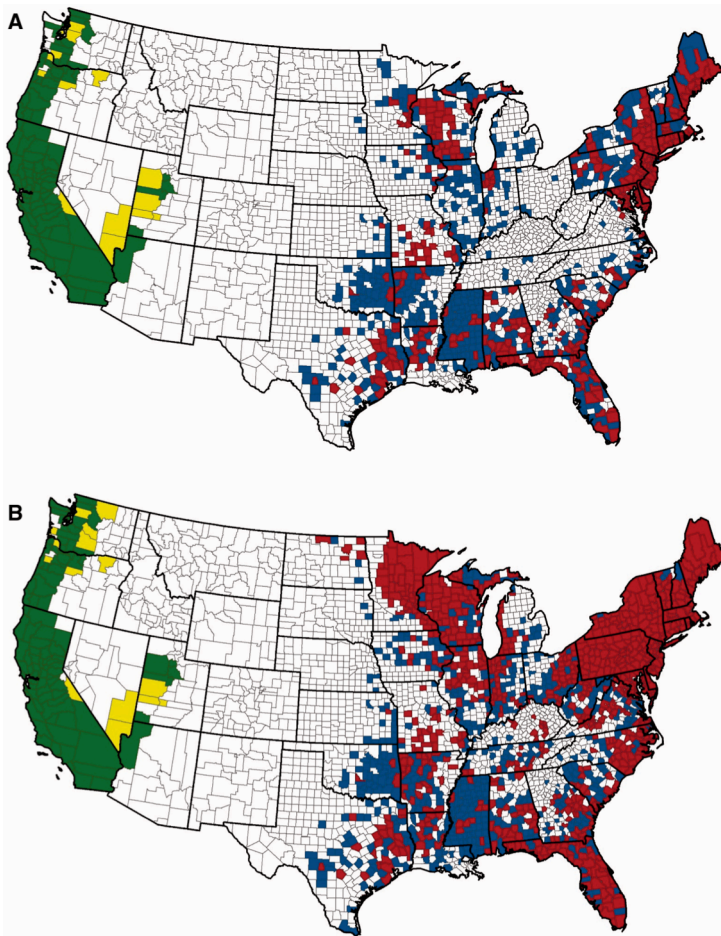


**Figure 1.2.** Incidence of Ticks in American counties 1907-1996(a), and 1907-2015(b). Red and green are 2+ confirmed cases; blue and yellow are 1. Published by Oxford University Press on behalf of Entomological Society of America 2016.<sup>5</sup>

disease have seen increased populations and range as a result of global climate change.<sup>4, 5</sup>

To mitigate such environmental harm and societal impacts, there has been a push for different energy sources that are less harmful. In particular, renewable energy sources have seen increases in investment and innovation<sup>2</sup>.

Renewable energy sources like wind, geothermal, and solar power have become icons of a new era of “green energy”<sup>1</sup>.

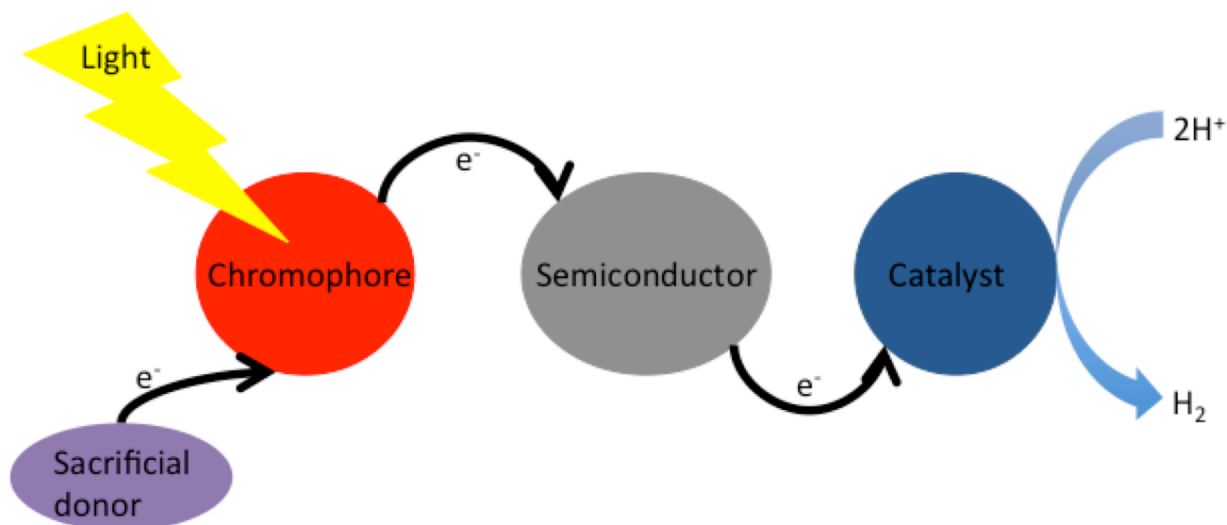
In particular, solar energy sources have immense untapped

potential for energy capture.<sup>6</sup> In fact, 407 quadrillion Btu of energy hit the Earth's surface every hour.<sup>6</sup> That means that less than two hours of sunlight has the potential to produce enough energy to satisfy human consumption for a year.

Currently, the majority of solar energy is harvested by photovoltaic cells, which do not have an intrinsic storage mechanism.<sup>6,7</sup> To truly tap into the ability of solar power, an easy, cheap storage and retrieval method will be necessary.<sup>6,8</sup> Theoretical methods include electric batteries, mechanical storage, and generation of solar fuels. Electric batteries are ideal, but currently there are no inexpensive, long-lived batteries that would work on the scale discussed.<sup>6</sup> Mechanical storage would involve something along the lines of pumping water uphill to store energy and letting it flow naturally to release it, but that would require the equivalent of 5,000 Hoover Dams. Thus, the best proposed solution to the storage problem is Artificial Photosynthesis (AP).

AP refers to the capture and immediate use of solar energy to form chemical bonds. In this way, it mimics nature, which uses light and water to reduce NADP<sup>+</sup> to NADPH and produce O<sub>2</sub> in Photosystems I and II.

AP generally involves a light-harvesting molecule called a chromophore, which absorbs light and excites an electron. The electron is then transferred to an electrocatalyst, which reduces one molecule to a usable fuel, like methane or hydrogen gas.<sup>8-10</sup> In a generic heterogeneous system as seen in scheme **1.1**, the electrocatalyst and chromophore are linked by a semiconductor or other immobilizing material, like a Metal-Organic Framework or polymer.<sup>8-10</sup> These are referred to as heterogeneous systems. They offer the ability to tailor systems for the task at hand, often leading to higher activity or more efficient systems.<sup>8,12</sup>

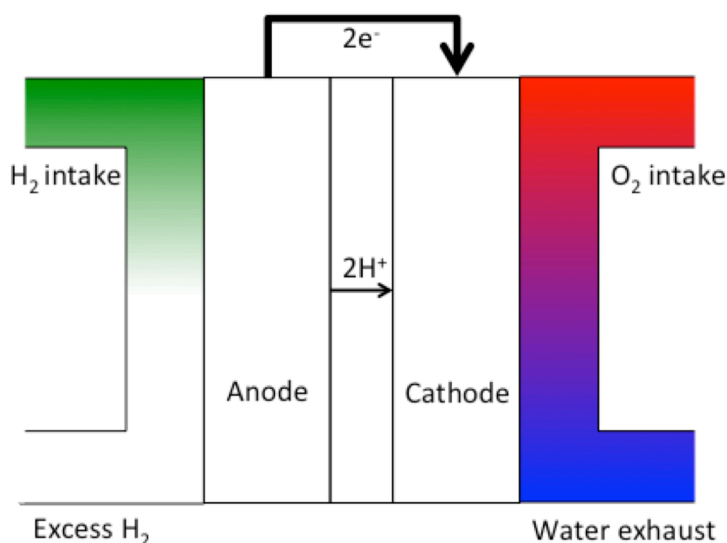


**Scheme 1.1** Artificial photosynthesis system, using a semiconductor as a mediating material between the chromophore and catalyst.

Homogenous systems lack immobilization; instead catalyst and chromophore are dissolved in solution. Research in homogeneous systems helps to discover the most efficient and most active catalysts, which will then be integrated into heterogeneous systems.<sup>12</sup> Additionally, the study of homogeneous catalysis provides greater insights into mechanistic factors surrounding the reactions of interest.<sup>12,13</sup> The development of homogeneously catalysts is crucial to future green energy needs in the field of AP. In order to keep catalysts inexpensive, the catalysts must be synthesized with earth abundant metals.

Once a working AP system is developed, the next challenge is efficient use of solar fuels. Traditional fuel use is through combustion, like coal burning on trains or oil in cars. Hydrogen gas has been similarly directly reacted with oxygen to fit a modified diesel engine,<sup>14</sup> but there are also promising next-generation energy technologies make extensive use of hydrogen gas.<sup>8-12</sup> Perhaps the most promising is the hydrogen fuel cell, for its





**Scheme 1.2** Illustration of a hydrogen fuel cell.

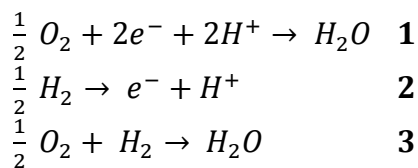
extremely clean system.

Hydrogen fuel cells convert gaseous hydrogen and oxygen into electricity, with only water as a byproduct,<sup>9</sup> as seen in Scheme 1.2.

In hydrogen fuel cells, two half-reactions occur, equations **1** and **2**. These reactions occur at the cathode

and anode respectively, and are separated by a salt bridge or electrolyte solution and a wire.<sup>8</sup> The net effect of the cell is equation **3**, and the flow of high-energy electrons from the anode to cathode.<sup>16</sup> Since one reactant is  $O_2$ , which is ubiquitous, the only necessary reactant is  $H_2$ . This technology has already been used to power cars,<sup>17</sup> and would be incredibly useful as an environmentally friendly power source.<sup>15-17</sup>

One of the main problems facing hydrogen fuel cells today is the necessity of efficient catalysts for both reactions. As the activation energy of specifically equation **2** is very high, development of a catalyst is an active area of research.<sup>8</sup> Traditional catalysts involve Pt-based compounds,<sup>8,15</sup> which are expensive, or biologically-inspired heme macrocycles.<sup>8</sup> This project seeks to investigate the potential of non-heme common earth metal catalysts for equation **3**, the oxygen reduction reaction (ORR).



The ideal electrocatalyst is selective, efficient, highly active, stable, and inexpensive. When designing and testing catalysts, we optimized for the first three criteria. Selectivity is reaction dependent; it is not a necessary consideration for proton reduction/hydrogen generation reactions, but is very important for ORR. Efficiency and activity are measured by overpotential and rate constants respectively. Overpotential is a measure of efficiency; it refers to the additional energy needed past the thermodynamic requirement to observe catalytic activity. Activity is a measure of how quickly a reaction proceeds, usually in terms of rate constants  $k_{\text{obs}}$  and  $k_{\text{cat}}$ ,<sup>8</sup> or in turnover frequency (TOF). TOF is the number of reactions per catalyst per unit time. The most common technique for determination of these constants is Cyclic Voltammetry (CV). CV induces a potential gradient in solution and measures the resulting current as a catalyst and substrate react. It allows for precise control of the energy injected into solution (the potential) and measurement of how much the reaction proceeds (the current).

Low cost and high activity electrocatalysts are required for the energy solutions of tomorrow. AP systems need better, less expensive catalysts to efficiently reduce protons, so they may become part of the future energy economy in a short time frame. Hydrogen fuel cells rely on the development of a suitable electrocatalyst for ORR for the same reasons. Thus it is important that common earth metal catalysts are developed with inexpensive ligand substituents. Under the pressure of eminent climate change disasters and rising energy demands, these solutions must be a priority.

## References

1. U.S. Energy Information Administration. (2017, September). "EIA predicts 28% increase in world energy use by 2040". From <https://www.eia.gov/todayinenergy/detail.php?id=32912>
2. U.S. Energy Information Administration. (2017, September). *International Energy Outlook 2016 –Executive Summary*.
3. U.S. Environmental Protection Agency. (2018). "Greenhouse Gas Emissions". From <https://www.epa.gov/ghgemissions/overview-greenhouse-gases>
4. U.S. Environmental Protection Agency. (2018). "Climate Change Indicators". From <https://www.epa.gov/climate-indicators>
5. R. J. Eisen, L. Eisen, C. B. Beard, County-Scale Distribution of *Ixodes scapularis* and *Ixodes pacificus* (Acari: Ixodidae) in the Continental United States. *J. Medical. Entomology*, **2016**, 53, 2, 349-386. Doi: 10.1093/jme/tjv237
6. Lewis, N. and Nocera, D. *PNAS*. **2006** 103 (43) 15729-15735.
7. International Energy Agency. Next Generation Wind and Solar. **2016**.
8. M. L. Pegis, C. F. Wise, D. J. Martin, and J. M. Mayer, *Chem. Rev.*, **2018**. 18 (5), 2340–2391.
9. D. Kim, K. K. Sakimoto, D. Hong, and P. Yang. *Angewandte Minireviews*, **2015**. 54 (11), 3259-3266
10. J. M. Ogden. *Annual Review of Energy and the Environment*. **1999**. 24, 227-279.
11. (a) A. C. Cavell, C. L. Hartley, D. Liu, C. S. Tribble; W. R. McNamara, *Inorg. Chem.* **2015**, 3325-3330, (b) G. P. Connor, K. J. Mayer, C. S. Tribble, W. R. McNamara, *Inorg. Chem.* **2014**, 53, 5408-5410, (c) C. L. Hartley, R. J. DiRisio, T. Y. Chang, W. Zhang, W. R. McNamara. *Polyhedron*, **2016**, 114, 133-137
12. S. Fukuzumi, Y. Lee, W. Nam., *Chem Cat Chem*, **2018**, 10 (1) 9-27..
13. W. Zhang, W. Lai, R. Cao, *Chem. Rev.*, **2017**, 117(4), 3717–3797
14. J. Excell. "UK firm to demonstrate "world's first" hydrogen-fuelled combustion engine truck". *The Engineer*. **2019**. From: <https://www.theengineer.co.uk/hydrogen-fuelled-combustion-engine-truck/>
15. G. Slaughter. Enzymatic Glucose Biofuel Cell and its Application. *Journal of Biochips and Tissue Chips*. **2015**. 5 (1).
16. M. L. Pegis, B. A. McKeown, N. Kumar, K. Lang, D. J. Wasylenko, X. P. Zhang, S. Rauegi and J. M. Mayer. *ACS Cent. Sci.* **2016**. 2 (11), 850–856.
17. S. Curtain, S. Gangi, *Fuel Cell Technologies Market Report 2016*; Department of Energy, Office of Energy Efficiency and Renewable Energy, Washington, D.C., **2016**.
18. V. Vij, S. Sultan, A. M. Harzandi, A. Meena, J. N. Tiwari, W. Lee, T. Yoon, K. S. Kim, *ACS Catalysis*, **2017**, 7 (10), 7196-7225
19. D. J. Wasylenko, C. Rodríguez, M. L. Pegis, and J. M. Mayer, *Chem. Rev.* **2014**, 136(36), 12544-12547.
20. S. Fukuzumi, S. Mochizuki, and T. Tanaka. *Inorg. Chem.* **1989**, 8 (12), 2459–2465.

## Chapter 2: Proton Reduction by Cobalt Schiff-base Complexes

### Introduction

Previously, our lab has reported that the Co catalyst with Schiff-base ligand **1** was active for proton reduction (equation 4).<sup>1</sup> An analog without the nitro group substituents was not.<sup>1</sup> For **1**, catalytic activity was moderate and efficiency was high,<sup>1</sup> but more importantly the use of a chiral 1,2-diaminocyclohexane backbone made our specific stereoisomer more difficult to isolate. We circumvented the problem by using (1R,2R)-diaminocyclohexane as a starting material, but that increased the cost of synthesis.

Here, I report complexes **2** and **3** as derivatives of **1**, which improve on catalytic performance while reducing the cost of synthesis. They lack the chiral backbone, using 1,2-ethylenediamine as a starting material instead. Like **1**, **2** and **3** are functionalized with

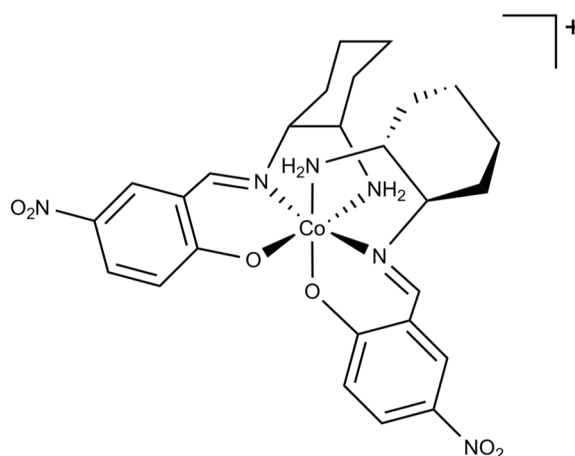


**Figure 2.1** Redox-active Co complex with cyclohexyl backbone.<sup>1</sup>

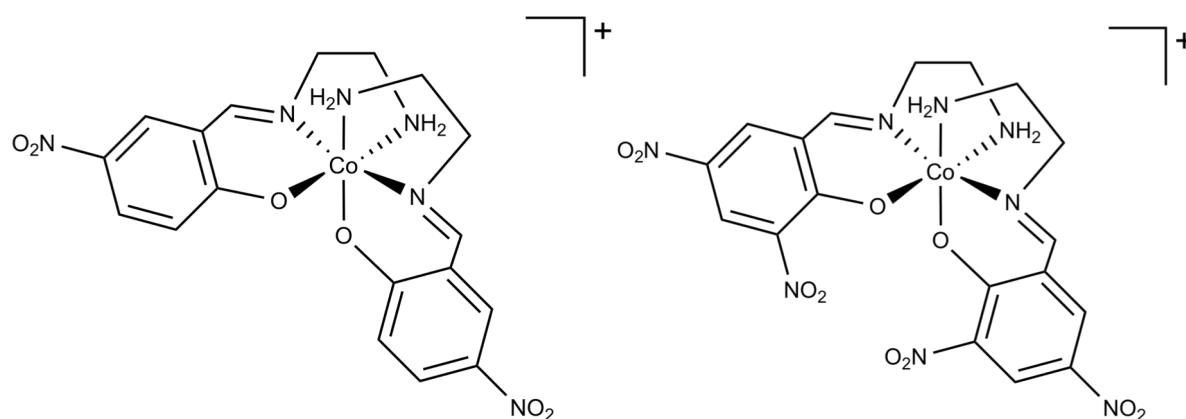
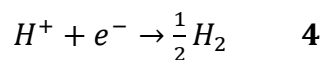


**Figure 2.2.** Cobalt dinitro-substituted (left, **2**) and tetranitro-substituted (right, **3**) complexes.

nitro substituent groups to withdraw electron density away from the metal center and subsequently lower overpotential. This chapter presents synthesis, characterization, and electrochemical analysis of **2** and **3**. X-ray diffractometry was used to characterize their crystal structure and Cyclic Voltammetry was used to determine efficiency and activity in terms of overpotential and rate constants, respectively.

CV, pictured in figure 2.3, is an electrochemical technique using three electrodes to induce and measure a current in a solution of interest. The working electrode induces potential, and the auxiliary or counter electrode measures the changes in current. The third electrode acts as an internal reference. As the reaction proceeds, the potential (in V) is varied, ideally giving a wave like in figure 2.4. Scan rate,  $\nu$ , is the rate of change in the potential per second.

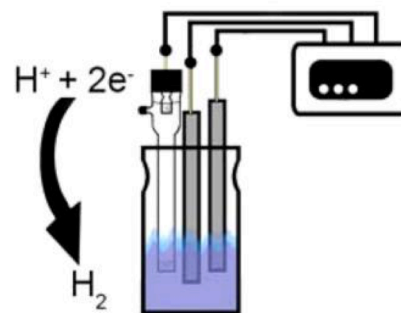


**Figure 2.3.** Setup of a CV experiment. A potentiostat maintains and measures the current in solution.<sup>9</sup>

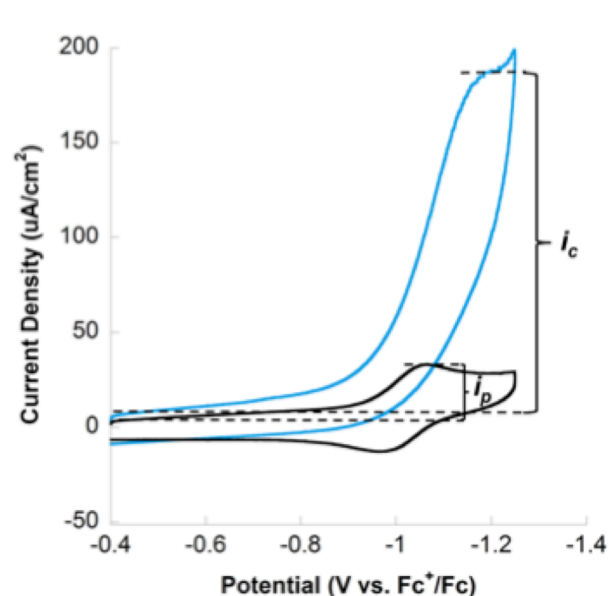


**Figure 2.4.** Example of CV experiment with  $i_p$  and  $i_c$  indicated. Blue is with acid, black is without.

For both **2** and **3**, catalytic activity and overpotential were measured by CV. In the absence of protons, the catalyst will undergo a reduction when scanned cathodically and oxidation when scanned anodically. This is the Co (III/II) couple seen at about -1 V in figure 2.4. Upon the addition of protons, an irreversible reduction wave is observed (blue in Figure 2.4). In this case, the couple corresponds to

the reduction of protons (reaction 4) by the catalyst.

From the initial CV, the first determination is the increase in the catalytic wave upon addition of a proton source. The peak current of the system without a proton source is called  $i_p$ , and the peak current of the catalytic wave is  $i_c$ . The ratio,  $i_c/i_p$ , is linked to the kinetic rate constant by the following derivation.<sup>3,4</sup>

Equation 5 is the Randles-Sevik equation for peak current of a diffusion-controlled reaction.<sup>4</sup> Equation 6 is an approximation for current depending on scan rate, and is mechanism dependant,<sup>3</sup> will be discussed in the results.

$$i_p = 0.4463FSC_p^0 \left( \frac{FvD}{RT} \right)^{\frac{1}{2}} \quad 5$$

$$i_c = \frac{nFSC_p^0 (Dk_{obs})^{\frac{1}{2}}}{1 + \exp\left(\frac{F}{RT}(E - E_{cat/2})\right)} \quad 6$$

$$\frac{i_c}{i_p} = \frac{n(k_{obs})^{\frac{1}{2}}}{0.4463} \left( \frac{Fv}{RT} \right)^{\frac{1}{2}} * \frac{1}{1 + \exp\left(\frac{F}{RT}(E - E_{cat/2})\right)} \quad 7$$

where  $i_p$  is the peak current;  $i$  is the current at a given potential,  $E$ ;  $F$  is Faraday's constant;  $R$  is the gas constant in J/mol K;  $n$  is the number of electrons transferred;  $E_{cat/2}$  is the half-wave potential;  $S$  is the surface area of the electrode;  $T$  is temperature;  $D$  is the diffusion coefficient, and  $C_p^0$  is the concentration of catalyst.

Note that the only quantities not directly measured by a CV or part of the experimental parameters are  $D$  and  $k_{obs}$ . Dividing equation 5 by 6 gives 7 which relates only known variables and allows solving for  $k_{obs}$  as a slope.<sup>3,4</sup>

Traditionally, the variable term in equation 7,  $\frac{1}{1+\exp\left(\frac{F}{RT}(E-E_{cat/2})\right)}$ , is excluded under the assumption of an ideal catalytic wave.<sup>1,4</sup> Ideal catalytic waves are S-shaped waves, shown in zone KS of figure 2.5. Since the potential at which  $i_c$  is measured is the current plateau, and the current plateau under ideal conditions is more than 100 mV away from  $E_{cat/2}$ ,  $E - E_{cat/2}$  becomes large and  $\frac{1}{1+\exp\left(\frac{F}{RT}(E-E_{cat/2})\right)}$  is approximately one.

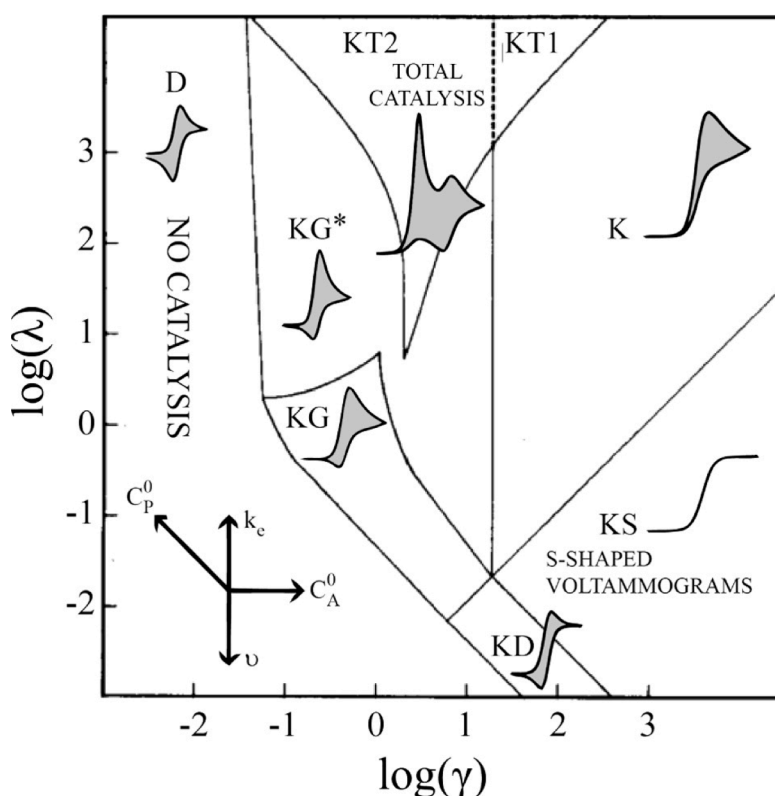


**Figure 2.5.** Categorizations of catalytic waves. Zone KS shows ideal behavior and zone K shows observed behavior. Courtesy of Elgrishi et. al.<sup>4</sup>

However, in experiment, ideal conditions are rarely met. The ideal curve indicates no side reactions or phenomena that disrupt the current. In particular, it assumes immediate substrate replacement at the electrode surface.<sup>4</sup> In reality, CV is limited to the diffusion rate of protons through solvent, which leads to a drop in current after the

maximum catalytic rate is achieved.<sup>4</sup> Observation of CVs in appendix A1-6 shows that our experiments exhibit this drop in current consistent with a duck shaped curve as in zone K of figure 2.5. In addition to the diffusion limit, catalyst decomposition and other side phenomena may cause non-ideal nature.

In recent years, Savéant and coworkers have developed Foot-of-the-Wave analysis (FOWA) to extract kinetic constants from the ideal portions of the catalytic wave (the “foot” of the wave, seen in figure 2.6).<sup>5</sup> Using equation 7, the  $i_c/i_p$  is plotted against

$\frac{1}{1+\exp\left(\frac{F}{RT}(E-E_{cat}/2)\right)}$ . The slope of the linear fit is a function of the rate-limiting step of the

reaction, which can be extracted by equation 8.

$$m = \frac{n(k_{obs})^{\frac{1}{2}}}{0.4463} \left(\frac{Fv}{RT}\right)^{\frac{1}{2}} \quad 8$$

From the slope,  $k_{obs}$  (in  $s^{-1}$ ) is extracted, and that is used to find the catalytic rate constant  $k_{cat}$  and the  $TOF_{max}$  by using equation 9.  $TOF_{max}$  is the maximum theoretical number of reactions per catalyst molecule per second in 1 M protons in units of  $s^{-1}$ .<sup>10</sup>

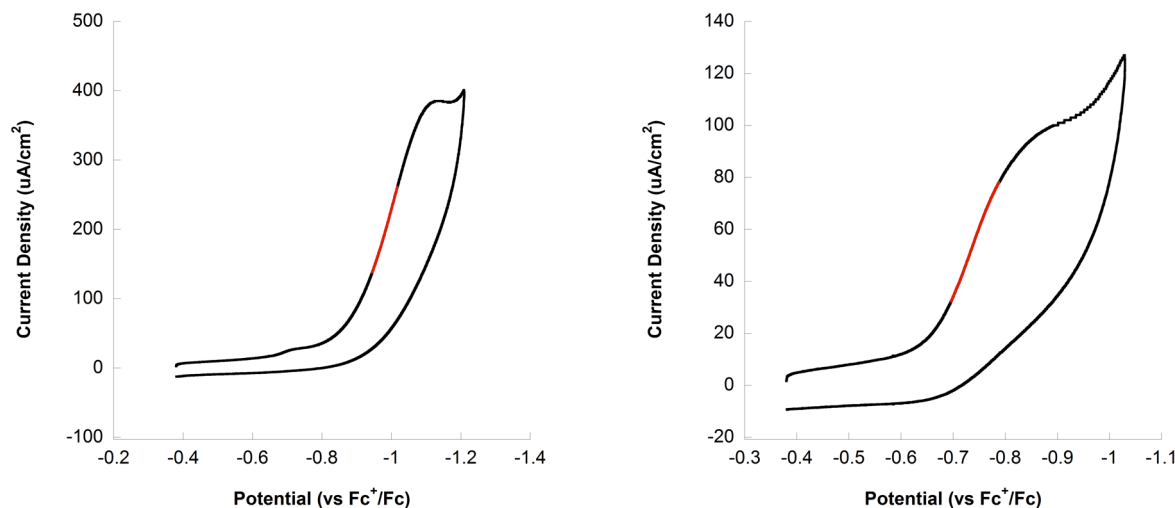


**Figure 2.6** Portions of the CV used for FOWA graph (black) for **2** (left) and **3** (right).



$$k_{obs} = \frac{k_{cat}}{[catalyst]} = \frac{TOF_{max}}{[catalyst]} * 1 M acid \quad 9$$

While  $TOF_{max}$  is an invaluable metric for activity of a catalyst, it does not measure efficiency. The second common metric, overpotential, is the potential difference between a theoretical maximum efficiency system and the half-wave potential of the observed system (see figure 2.7). The thermodynamic potential is unique to the solvent acid pair, and is often the subject of debate, as experimental determination of reduction potential of an acid in an organic solvent is difficult because of homoconjugation and shift in  $pK_a$ .<sup>4</sup> Additionally, non-ideal wave behavior can lead to inaccuracies in determination of half-wave potential.<sup>4</sup> Overpotential is calculated from equation 10, where  $\eta$  is the overpotential in V and  $E_{therm}$  is the thermodynamic potential of the reaction.

$$\eta = E_{therm} - E_{cat/2} \quad 10$$

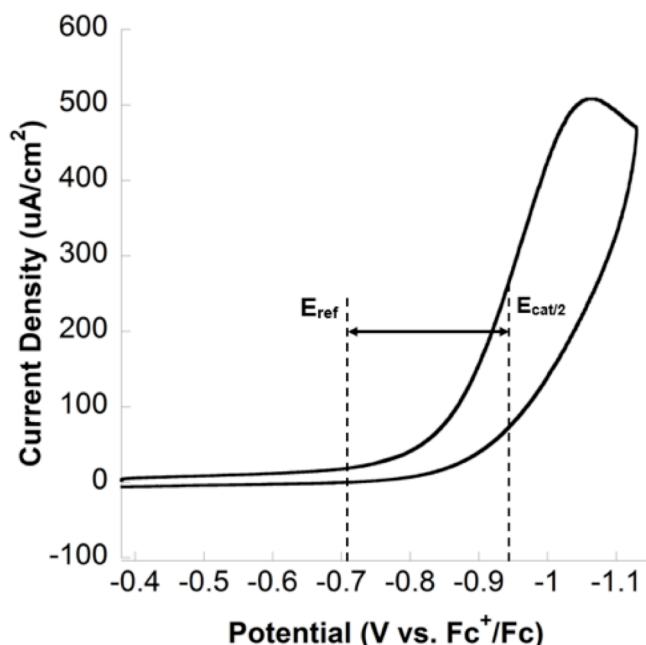


**Figure 2.7.** Overpotential is determined by the difference between the half wave potential of the irreversible catalytic event and the  $E_{therm}$  or  $E_{ref}$  for the acid-solvent pair.<sup>2</sup>

Together, the  $TOF_{\max}$  and overpotential are good metrics of catalyst activity and efficiency. To demonstrate the relationship between the two, we generate Tafel plots, seen in figure 2.8. Equation 11 shows the calculation for the TOF at values other than the catalytic wave, and is primarily used to compare the reaction rates at zero overpotential, which allows for comparison between dissimilar systems (either because overpotentials are widely different, or across homogenous/heterogeneous systems).<sup>6</sup> TOF at zero overpotential represents the catalyst at theoretical ideal behavior with respect to efficiency. This is useful for benchmarking the catalyst in relation to other homogeneous and heterogeneous catalyst.<sup>6</sup> Equations used to derive the plot are below, where  $E$  is the varying potential.

$$TOF = \frac{TOF_{\max}}{1 + \exp\left(\frac{F}{RT}(E - E_{cat/2})\right)} \quad \mathbf{11}$$

$$TOF = \frac{TOF_{\max}}{1 + \exp\left(\frac{F}{RT}(E_{therm} - \eta - E_{cat/2})\right)} \quad \mathbf{12}$$

Equation 11 gives the TOF at a varying potential. Overpotential at that same potential can be calculated, as seen in equation 10. Substituting 10 in 11 gives 12, which can be graphed to make a Tafel plot (figure 2.8). This is typically done with a logarithmic transformation for TOF.

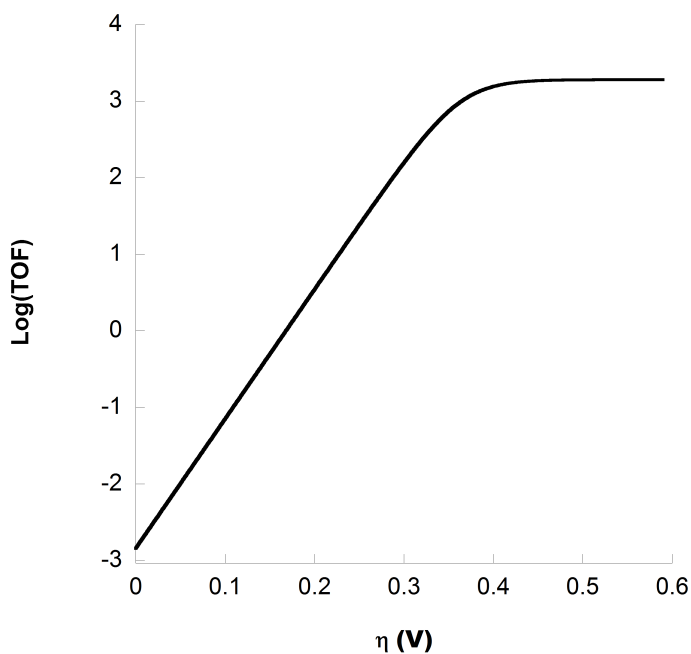


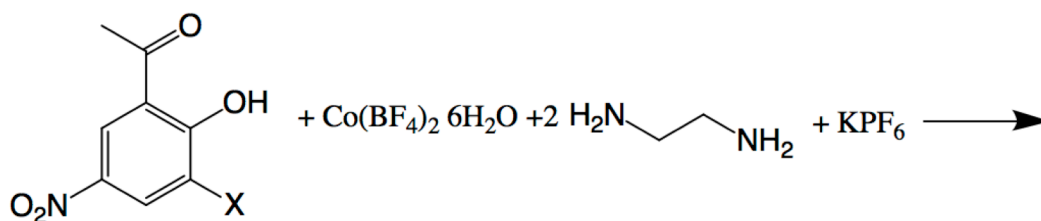
**Figure 2.8.** Tafel plot of **2** at  $v = 200$  mV/s.

In order to construct efficient, scalable AP systems, inexpensive and simply synthesized proton reduction electrocatalysis are needed. We will synthesize and investigate two novel Co catalysts for this reaction. Using the recently developed techniques of FOWA and Tafel plots, we will describe their ideal electrocatalytic behavior in terms of TOF and overpotential to facilitate comparison with other catalysts.

## Experimental Methods

### Materials

2-Hydroxy-5-nitrobenzaldehyde, tetra-n-butylammoniumhexa- fluorophosphate (98%), ethylenediamine, and potassium hexafluorophosphate were purchased from Acros Organics. Cobalt(II) tetrafluoroborate hexahydrate was purchased from Aldrich. 3,5-Dinitrosalicylaldehyde was purchased from Alfa Aesar. All other reagents were purchased from Fischer Scientific and used without further purification.<sup>2</sup>



**Scheme 2.1.** Synthesis of **2** and **3**. For **2**, X = H. For **3**, X =  $\text{NO}_2$ .

**Synthesis of 2.** Cobalt(II) tetrafluoroborate hexahydrate (255 mg, 0.75 mmol), 2-hydroxy-5-nitrobenzaldehyde (250 mg, 1.5 mmol), ethylene diamine (0.1 mL, 1.5 mmol), and potassium hexafluorophosphate (138 mg, 0.75 mmol) were dissolved in 50 mL of methanol. The solution was refluxed for 2 hours. The resulting solution was cooled to room temperature and filtered through Celite to remove impurities. The filtrate was collected and the solvent evaporated to dryness. A minimum amount of methanol was added until fully dissolved and a clear solution was found. The solution was layered above toluene to slowly diffuse the complex out of solution. After two days, dark brown crystals were extracted (85% yield). MS:  $m/z$  expected = 475.077084;  $m/z$  found = 475.07690. Elemental Analysis Calculated for  $\text{CoC}_{18}\text{H}_{20}\text{F}_6\text{N}_6\text{O}_6\text{P}$ : C, 34.85%; H, 3.25%; N, 13.55%. Found: C, 34.74%; H, 3.32%; N, 13.61%.  $^1\text{H}$  NMR (DMSO)  $\delta$ : 8.82 (2H, s); 8.52(2H,d,J=3.1Hz);

7.89(2H,dd,J1=3.1Hz,J2=9.4Hz); 6.66 (2H, d, J = 9.4 Hz); 4.51 (4H, m); 4.23 (2H, m); 4.08 (2H, m); <sup>13</sup>C NMR (DMSO) δ: 170.8, 167.0, 135.7, 132.5, 128.6, 122.8, 119.6, 62.2, 42.2.<sup>2</sup>

**Synthesis of 3.** Cobalt(II) tetrafluoroborate hexahydrate (255 mg, 0.75 mmol ), 3,5-dinitrobenzaldehyde (312 mg, 1.5 mmol), ethylene diamine (0.1 mL, 1.5 mmol) were dissolved in 50 mL of methanol. The solution refluxed for 2 hours and then was let cool to room temperature. The resulting solution was filtered through Celite to remove precipitate and the filtrate was collected. The solvent was removed under reduced pressure, and resulting solid was dissolved in the minimum amount of methanol required then layered above toluene. After two days, reddish-brown crystals were extracted (yield = 56%). MS: m/z expected = 565.047240; m/z found = 565.046860. Elemental Analysis Calculated for CoC<sub>18</sub>H<sub>20</sub>F<sub>6</sub>N<sub>8</sub>O<sub>10</sub>P: C, 33.15%; H, 2.78%; N, 17.18%. Found: C, 33.28%; H, 2.86%; N, 17.29%. <sup>1</sup>H NMR (DMSO) δ: 9.01 (2H, s); 8.81 (2H, d, J = 3.0 Hz); 8.57 (2H, d, J = 3.0 Hz); 4.96 (4H, s); 4.32 (2H, m); 4.17 (2H, m); <sup>13</sup>C NMR (DMSO) δ: 166.7, 162.0, 142.8, 134.9, 133.9, 125.9, 125.1, 42.4, 21.9.<sup>2</sup>

### **X-Ray diffractometry**

Single Crystal X-Ray Diffractometry was performed by William W. Brennessel at the X-Ray Crystallographic Facility at the University of Rochester. Analysis was performed using a Bruker SMART APEX II CCD platform diffractometer.<sup>2</sup>

**Characterization of 2.** A crystal (0.48 × 0.20 × 0.12 mm<sup>3</sup>) was placed onto the tip of a thin glass optical fiber and mounted on a Bruker SMART APEX II CCD platform diffractometer for a data collection at 100.0(5) K.<sup>7</sup> A preliminary set of cell constants and an orientation matrix were calculated from reflections harvested from three orthogonal

wedges of reciprocal space. The full data collection was carried out using MoK $\alpha$  radiation (graphite monochromator) with a frame time of 10 seconds and a detector distance of 3.99 cm. A randomly oriented region of reciprocal space was surveyed: twelve major sections of frames were collected with 0.50° steps in  $\omega$  at twelve different  $\varphi$  settings and a detector position of  $-38^\circ$  in  $2\theta$ . The intensity data were corrected for absorption.<sup>8</sup> Final cell constants were calculated from the xyz centroids of 3983 strong reflections from the actual data collection after integration.<sup>9</sup> See Table A1 for additional crystal and refinement information.<sup>2</sup>

**Characterization of 3.** A crystal (0.48 × 0.20 × 0.12 mm<sup>3</sup>) was placed onto the tip of a thin glass optical fiber and mounted on a Bruker SMART APEX II CCD platform diffractometer for a data collection at 100.0(5) K.<sup>7</sup> A preliminary set of cell constants and an orientation matrix were calculated from reflections harvested from three orthogonal wedges of reciprocal space. The full data collection was carried out using MoK $\alpha$  radiation (graphite monochromator) with a frame time of 10 seconds and a detector distance of 3.98 cm. A randomly oriented region of reciprocal space was surveyed: seven major sections of frames were collected with 0.50° steps in  $\omega$  at seven different  $\varphi$  settings and a detector position of  $-38^\circ$  in  $2\theta$ . The intensity data were corrected for absorption.<sup>8</sup> Final cell constants were calculated from the xyz centroids of 3787 strong reflections from the actual data collection after integration.<sup>9</sup> See Table A1 for additional crystal and refinement information.<sup>2</sup>

### **Cyclic Voltammetry**

Experiments were performed with a CH Instruments 620D potentiostat and a CH Instruments 680 amp booster. They used a vitreous carbon working electrode (radius 1.5

mm) and a Pt auxiliary electrode. Electrodes were polished between scans with 0.05  $\mu\text{m}$  alumina/water paste on a cloth covered tile, then rinsed with water and further polished with a solvent-soaked paper towel. Scans were carried out against a SCE reference electrode and ferrocene was used as an internal standard against reference electrode drift. All potentials listed here are against the  $\text{Fc}^+/\text{Fc}$  couple unless otherwise indicated. All experiments used an Ar atmosphere. Unless otherwise noted, added acid was trifluoroacetic acid (TFA).<sup>2</sup>

### **Acid Addition Studies**

Cyclic Voltammograms were obtained using 0.5 mg of crystal in 5.0 mL MeCN and 0.1 M TBAPF<sub>6</sub>. That corresponds to concentrations of 0.21 mM of **2** and 0.18 mM of **3**. CVs were obtained at 25° C, at various scan rates and concentrations of TFA. All studies included a background scan with no TFA in an Ar atmosphere. Ferrocene was used as an internal standard.<sup>2</sup>

### **Catalyst Concentration Studies**

2.5 mM stock solutions of **2** and **3** were prepared in MeCN. In an electrochemical cell, 0.1 M TBAPF<sub>6</sub> was dissolved in MeCN. Ferrocene was added as an internal standard. 44 mM TFA was added and the solution was degassed for 12 minutes with Ar. CVs were obtained at varying concentrations of **2** and **3** using their stock solutions at  $v = 200 \text{ mV/s}$ .<sup>2</sup>

## Results and Discussion

Complexes **2** and **3** were synthesized in a one-pot reaction in air. Upon successful synthesis, NMR, mass spectrometry and X-ray crystallography were all used to show the structure was exactly as theorized.

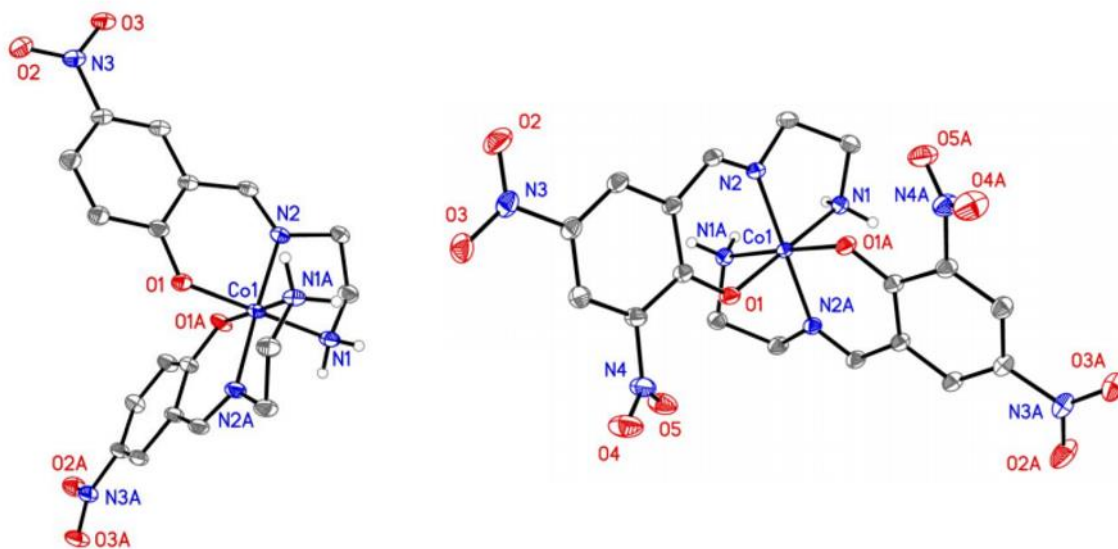


**Figure 2.9.** ORTEPs from X-Ray Crystallography of **2** (left) and **3** (right). PF<sub>6</sub> molecules are excluded for clarity.

After characterization, the next step was electrochemical analysis. CVs of **2** and **3** show reversible redox couples, corresponding to Co (II/I) reduction and oxidation, at -0.92 V vs. Fc<sup>+</sup>/Fc, and at -0.74 V vs. Fc<sup>+</sup>/Fc, respectively. The potential of these events is lower than that of **1**, indicating low overpotentials for both **2** and especially **3**.

Catalyst	$i_c/i_p$	$E_{cat/2}$ (V vs Fc <sup>+</sup> /Fc)	Overpotential (mV)
<b>2</b>	7.5	-1.2	280
<b>3</b>	5.5	-1.0	120

**Table 1.** Electrochemical analysis metrics summary for **2** and **3** when scan rate = 200 mV/s



Upon addition of acid, a catalytic response was observed from both **2** and **3**. In both cases, the catalytic response measured by  $k_{obs}$  increases linearly with acid, indicating first-order dependence on  $[H^+]$  (see s A5-A6). The acid used in all cases was Trifluoroacetic acid (TFA) because of its low background activity over the desired potential range. The catalytic response observed was also linear when concentrations of **2** and **3** were varied, suggesting a first order dependence on catalyst concentration. These determinations allow us to use equations 5-7 in later analysis<sup>4</sup>.

The next important consideration is mechanism. Possible mechanisms for this reaction all involve two reduction or electrical (E) events and two protonation or chemical (C) events. Electric events refer to electron movement, and chemical events are making an breaking of chemical bonds.<sup>2</sup>

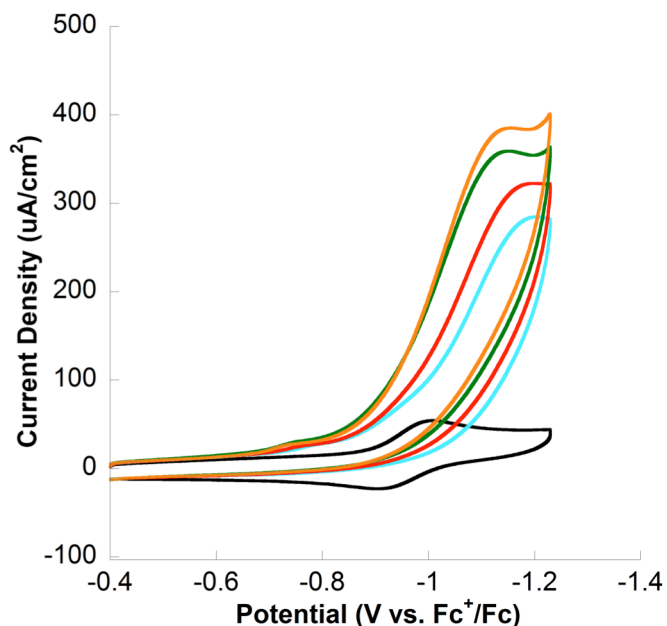


**Figure 2.10** CVs of 0.21 mM **2** in  $CH_3CN$  with 0.1M  $TBAPF_6$  (black) upon addition of 0.88 mM (blue), 1.76 mM (red), 2.42 mM (green), 3.08 mM (orange) of TFA at  $v = 200$  mV/s.<sup>2</sup>

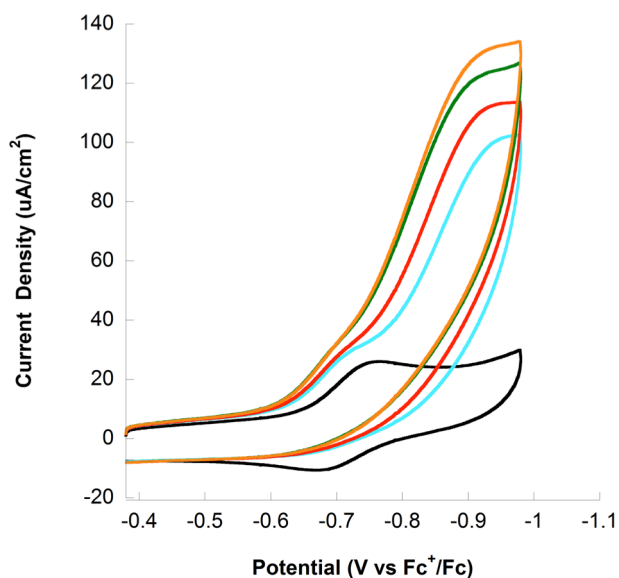


**Figure 2.11** CVs of 0.18 mM **3** in  $CH_3CN$  with 0.1M  $TBAPF_6$  (black) upon addition of 0.22 mM (blue), 0.44 mM (red), 0.66 mM (green), 0.88 mM (orange) of TFA at  $v = 200$  mV/s.<sup>2</sup>

Possible mechanisms are thus EECC, ECEC, ECCE, CCEE, or CECE. The acid addition studies show a single reduction event just before the catalytic wave, indicating the first step is an electric step and the second is a chemical one. Finally, for an EECC mechanism, the half-wave potential must be shifted no more than 17.6 mV positive of the catalyst's redox couple,<sup>7,8</sup> but we observe a shift of 50-99 mV. Hence we have an ECEC mechanism. Since the small reduction event merges with the larger catalytic reduction at high acid concentrations, we may also conclude that the second reduction step is more difficult than the first,<sup>7</sup> indicating the second reduction step is the rate-determining step. This indicates that equation 3 indeed models our  $i_c$ , and that FOWA analysis gives the  $k_{obs}$  for our second reduction step.

CV for **2** and **3** were transformed in line with equations 5-7 for FOWA analysis. The linear portion of the transformation, seen in figure 2.12, was generally between 0.2 and 0.8 for both. This portion of the wave was selected because it was the largest section of

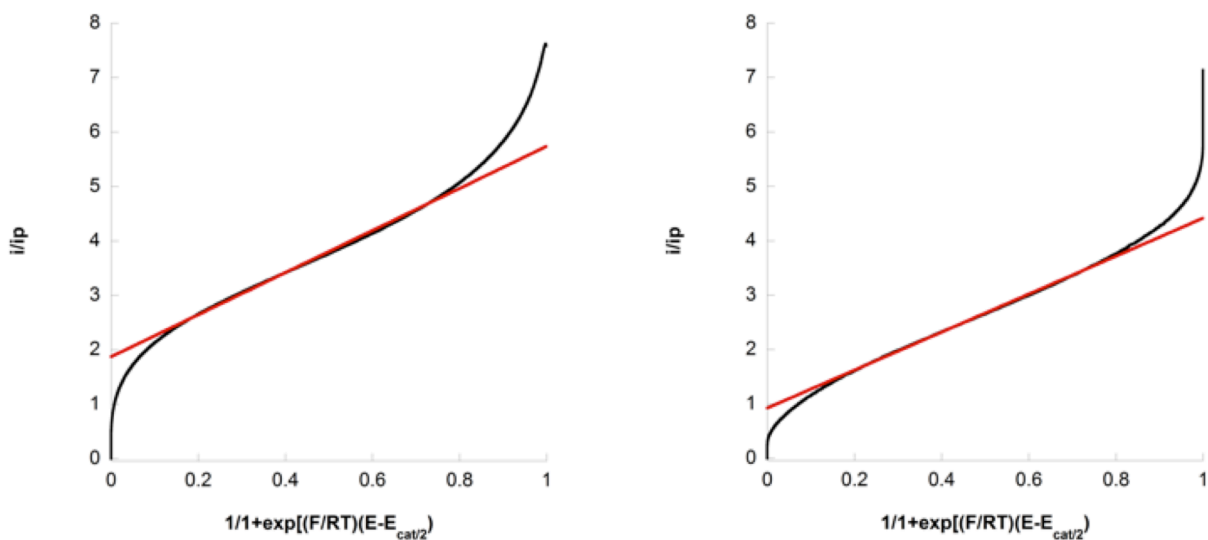


**Figure 2.12** Linear fit (red) for FOWA graph (black) for **2** ( $R^2 = 0.99$ ) and **3** ( $R^2 = 0.99$ ).

linearity, and corresponded to roughly the appropriate  $i_c/i_p$  values. Existing literature have used the lowest linear portion of the transformation, seen where  $i_c/i_p < 1$  in figure **2.12**.

The observed rate constant of the rate-determining step,  $k_{obs}$ , of the reaction was extracted from the slope of the linear fit according to equation **8**. Values of  $k_{cat}$  and  $TOF_{max}$  were then found. For **2** and **3**, this gives theoretical  $TOF_{max}$  values of  $2100\text{ s}^{-1}$  and  $4100\text{ s}^{-1}$  respectively. These are not observed directly as experimental systems had at most 3.08 mM TFA, under which we observed experimental TOF values of  $7\text{ s}^{-1}$  for **2** and  $3\text{ s}^{-1}$  for **3**. To further benchmark these catalysts, we combined  $TOF_{max}$  with overpotential as described earlier in this chapter to generate Tafel plots (Figures A9-A15). These Tafel plots show that the TOF values at 0 overpotential and in a 1 M TFA system are  $0.001\text{ s}^{-1}$  for **2** and  $1.07\text{ s}^{-1}$  for **3**.<sup>2</sup>

We report two cobalt complexes that are active for proton reduction. They are inexpensive and synthesize in good yield. Addition of nitro-substituents lowered the overpotential of the catalysts to as low as 120 mV. FOWA and Tafel plots were used to find  $TOF_{max}$  and TOF at 0 overpotential of up to  $4100\text{ s}^{-1}$  and  $1.07\text{ s}^{-1}$  respectively. These analyses benchmarked the catalysts for comparison with other systems.

## References

1. J. Armstrong, P. Crossland, M. Frank, M. Van Dongen, and W. Mcnamara. **2016**. *Dalton Trans.*, 45(13), 5430-5433.
2. R. J. DiRisio, J. E. Armstrong, M. A. Frank, W. R. Lake and W. R. McNamara. **2017**, *Dalton Trans.* 46, 10418-10425
3. E. Rountree, B. Mccarthy, T. Eisenhart, and J. Dempsey. **2014**. *Inorg. Chem.*, 53(19), 9983-10002.
4. N. Elgrishi , M. B. Chambers and M. Fontecave. **2015**. *Chem. Sci.* 6, 2522-2531
5. C. Costentin, S. Drouet, M. Robert, and J. & Savéant. *J. Am. Chem. Soc.*, **2012** 134(27), 11235-42.
6. M. L. Pegis, C. F. Wise, D. J. Martin, and J. M. Mayer. *Chem. Rev.*, **2018**. 18 (5), 2340–2391.
7. C. Costentin, J. M. Savéant. Multielectron, *ChemElectroChem* **2014**, 1, 1226– 1236.
8. A. G. Maher, G. Passard, D. K. Dogutan, R. L. Halbach, B. L. Anderson, C. J. Gagliardi, M. Taniguchi, J. S. Lindsey and D. G. Nocera, *ACS Catal.*, **2017**, 7, 3597–3606.
9. A. C. Cavell, C. L. Hartley, D. Liu, C. S. Tribble, and W. R. McNamara. *Inorg. Chem.*, **2015**, 54 (7), 3325–3330
10. V. Artero and J.-M. Savéant, *Energy Environ. Sci.*, **2014**, 7, 3808–3814.

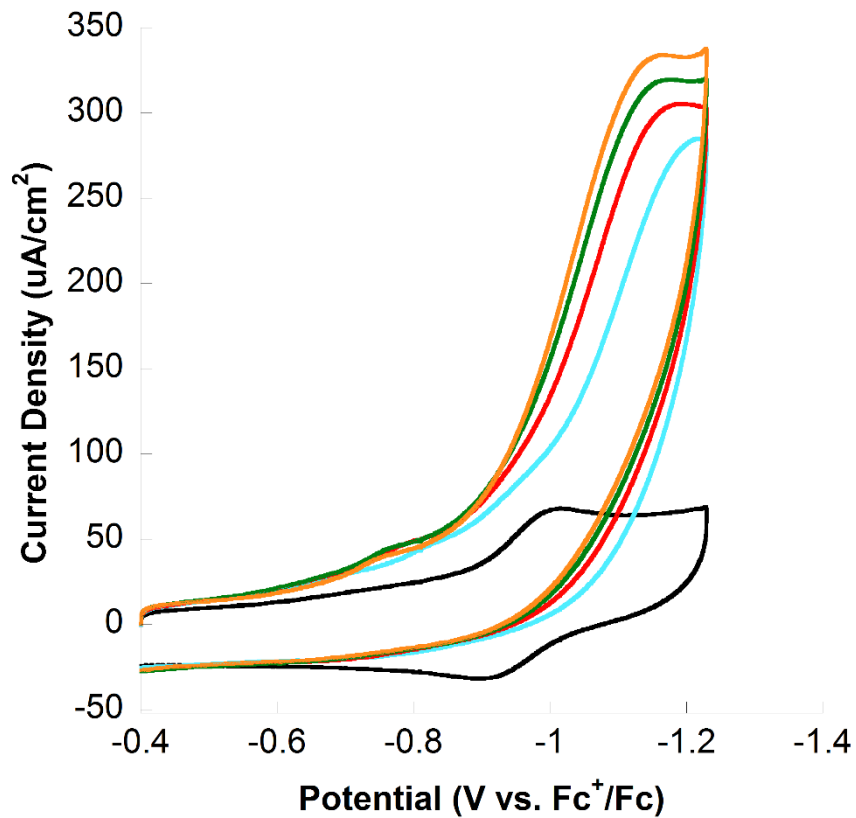
## Appendix A

**Table A1.** Selected bond lengths [ $\text{\AA}$ ] and angles [ $^\circ$ ].<sup>2</sup>

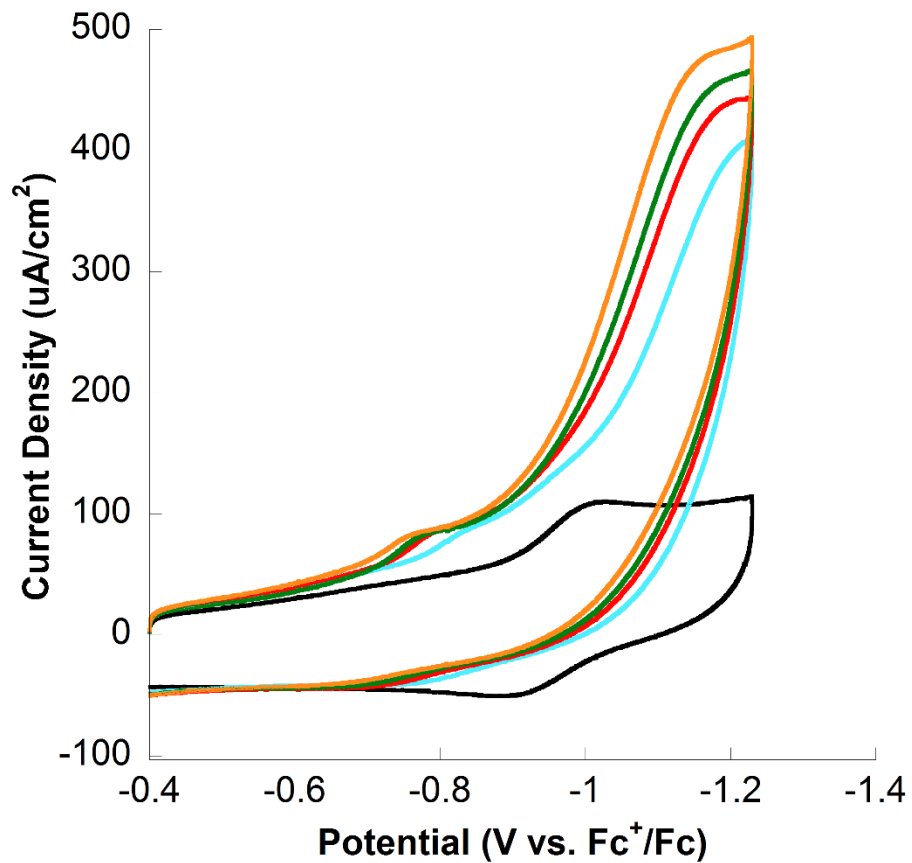
Bond Lengths ( $\text{\AA}$ ) for <b>2</b>		Bond Lengths ( $\text{\AA}$ ) for <b>3</b>	
Co1-O(1)	1.8940(9)	Co1-O(1)	1.8959(9)
Co1-O(1A)	1.8940(9)	Co1-O(1A)	1.8958(9)
Co1-N(1)	1.9600(11)	Co1-N(1)	1.9540(10)
Co1-N(1A)	1.9600(11)	Co1-N(1A)	1.9541(10)
Co1-N(2)	1.9024(10)	Co1-N(2)	1.9029(10)
Co1-N(2A)	1.9025(10)	Co1-N(2A)	1.9029(10)
N(2)-C(3)	1.2837(15)	N(2)-C(3)	1.2818(15)

Bond Angles ( $^\circ$ ) for <b>2</b>		Bond Angles ( $^\circ$ ) for <b>3</b>	
O(1)-Co1-N(2)	94.35(4)	O(1)-Co1-N(2)	94.05(4)
O(1)-Co1-N(2A)	87.49(4)	O(1)-Co1-N(2A)	87.24(4)
O(1A)-Co1-O(1)	91.20(6)	O(1A)-Co1-O(1)	89.61(6)
O(1A)-Co1-N(2A)	94.35(4)	O(1A)-Co1-N(2A)	94.05(4)
O(1A)-Co1-N(2)	87.49(4)	O(1A)-Co1-N(2)	87.24(4)
O(1A)-Co1-N(1)	87.51(4)	O(1A)-Co1-N(1)	88.08(4)
O(1)-Co1-N(1)	178.66(4)	O(1)-Co1-N(1)	177.62(4)
N(2)-Co1-N(2A)	177.37(6)	N(2)-Co1-N(2A)	178.18(6)



**Figure A1.** CV of 0 mM (Black), 0.77 mM (Blue), 1.54 mM (Red), 2.31 mM (Green), 3.08 mM (Orange) of TFA with 0.5 mg of **2** and 0.1 M TBAPF<sub>6</sub> at  $\nu = 500$  mV/s in MeCN.



**Figure A2.** CV of 0 mM (Black), 0.77 mM (Blue), 1.54 mM (Red), 2.31 mM (Green), 3.08 mM (Orange) of TFA with 0.5 mg of **2** and 0.1 M TBAPF<sub>6</sub> at  $\nu = 1$  V/s in MeCN.

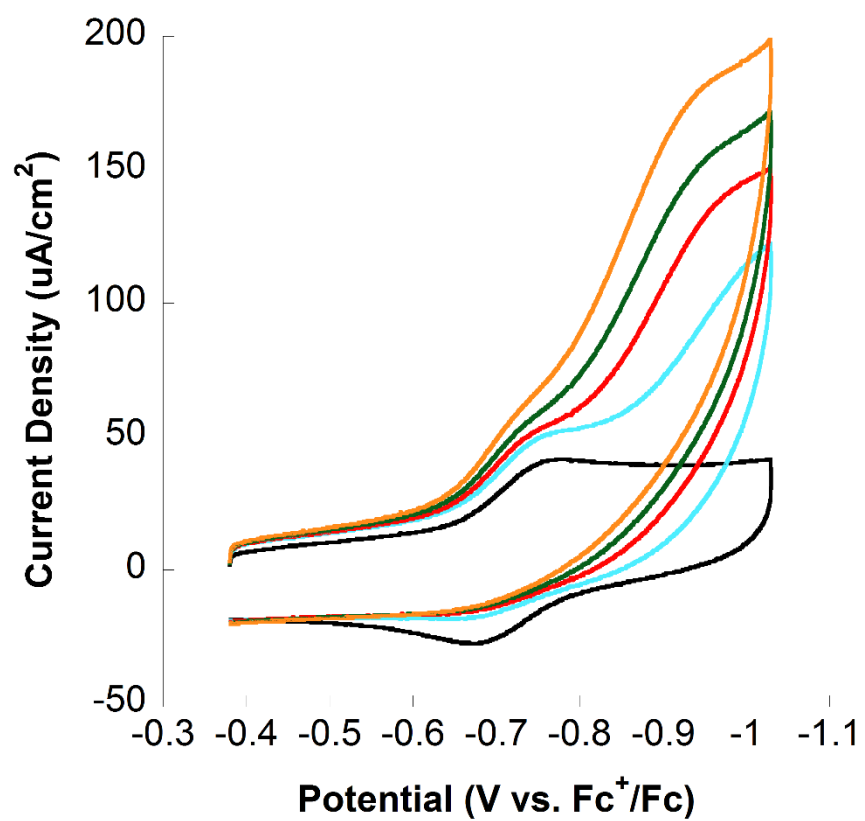


**Figure A3.** CV of 0 mM (Black), 0.22 mM (Blue), 0.44 mM (Red), 0.66 mM (Green), and 0.88 mM (Orange) of TFA with 0.5 mg of **3** and 0.1 M  $\text{TBAPF}_6$  at  $v = 600$  mV/s in MeCN.



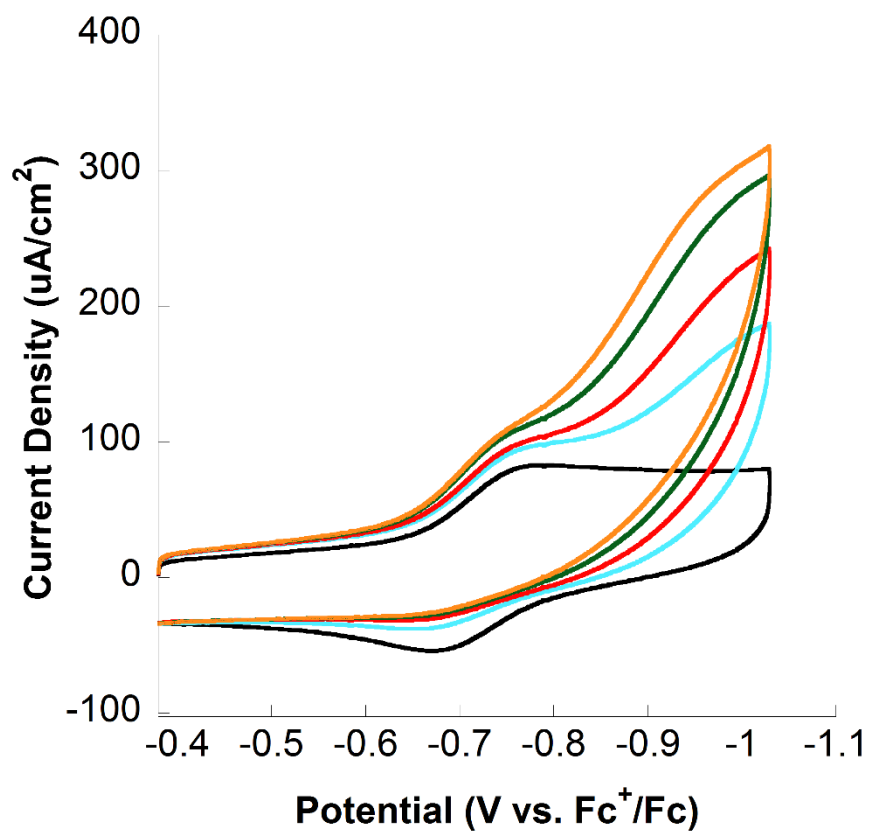


**Figure A4.** CV of 0 mM (Black), 0.22 mM (Blue), 0.44 mM (Red), 0.66 mM (Green), and 0.88 mM (Orange) of TFA with 0.5 mg of **3** and 0.1 M TBAPF<sub>6</sub> at  $v = 1$  V/s in MeCN.

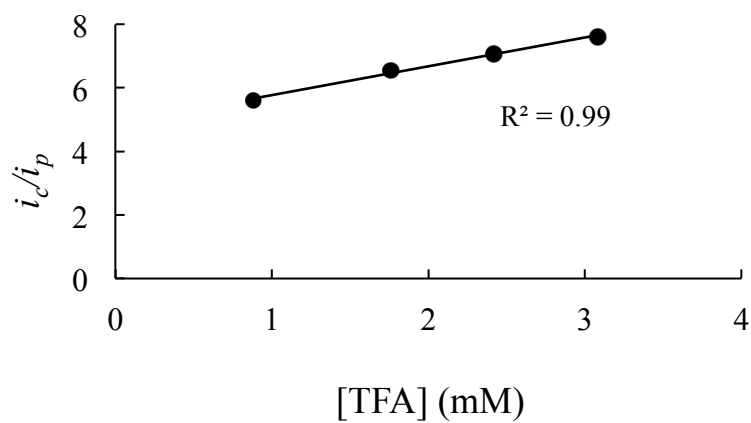


**Figure A5.** The  $i_c/i_p$  vs. [TFA] for CVs of 0.5 mg of **2** in CH<sub>3</sub>CN upon addition of 0.88 mM, 1.76 mM, 2.42 mM, and 3.08 mM TFA at  $v = 200$  mV/s was fit with a linear correlation.<sup>2</sup>

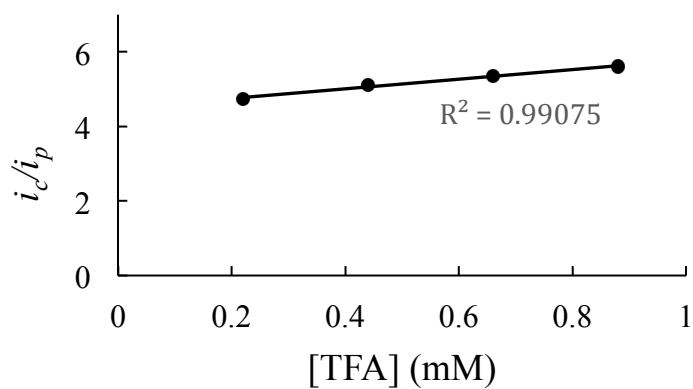


**Figure A6.** The  $i_c/i_p$  vs. [TFA] for CVs of 0.5 mg of **3** in CH<sub>3</sub>CN upon addition of 0.22 mM, 0.44 mM, 0.66 mM, and 0.88 mM TFA at  $v = 200$  mV/s was fit with a linear correlation.<sup>2</sup>

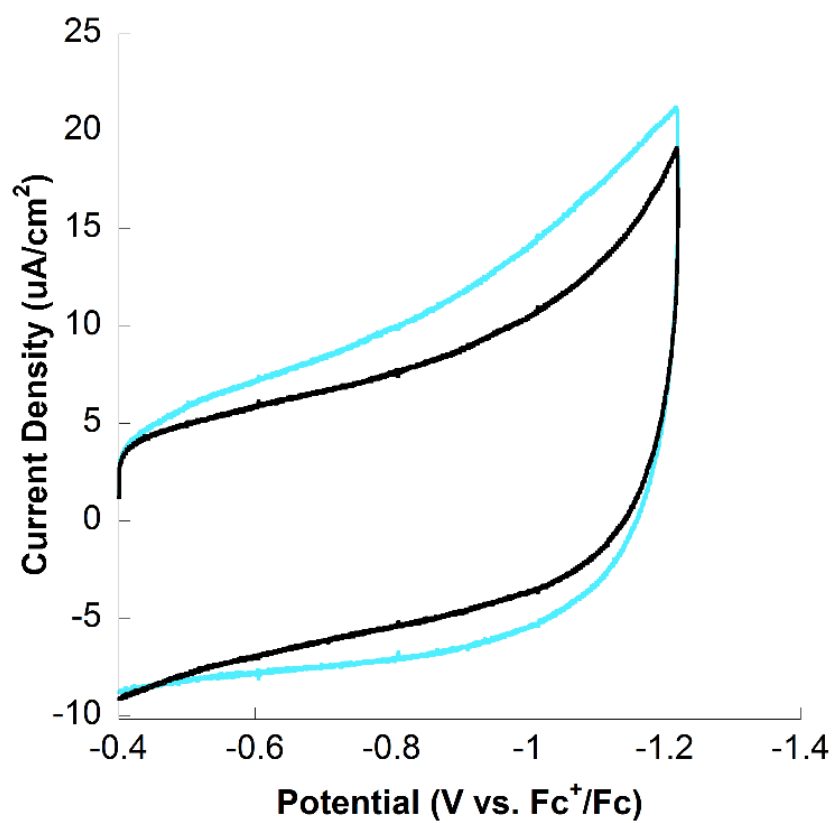


**Figure A7.** CVs of 0.1 M TBAPF<sub>6</sub> in CH<sub>3</sub>CN without TFA (Black) and addition of 13.2 mM TFA (Blue) in the range of 2.<sup>2</sup>

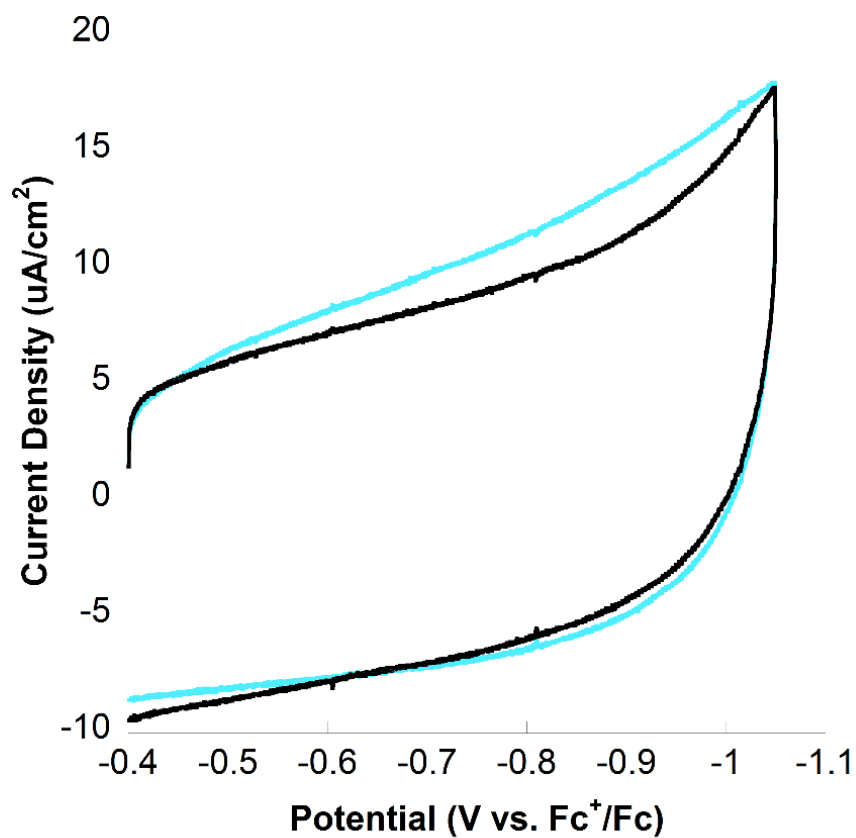


**Figure A8.** CVs of 0.1 M TBAPF<sub>6</sub> in CH<sub>3</sub>CN without TFA (Black) and addition of 13.2 mM TFA (Blue) in the range of **3**.<sup>2</sup>

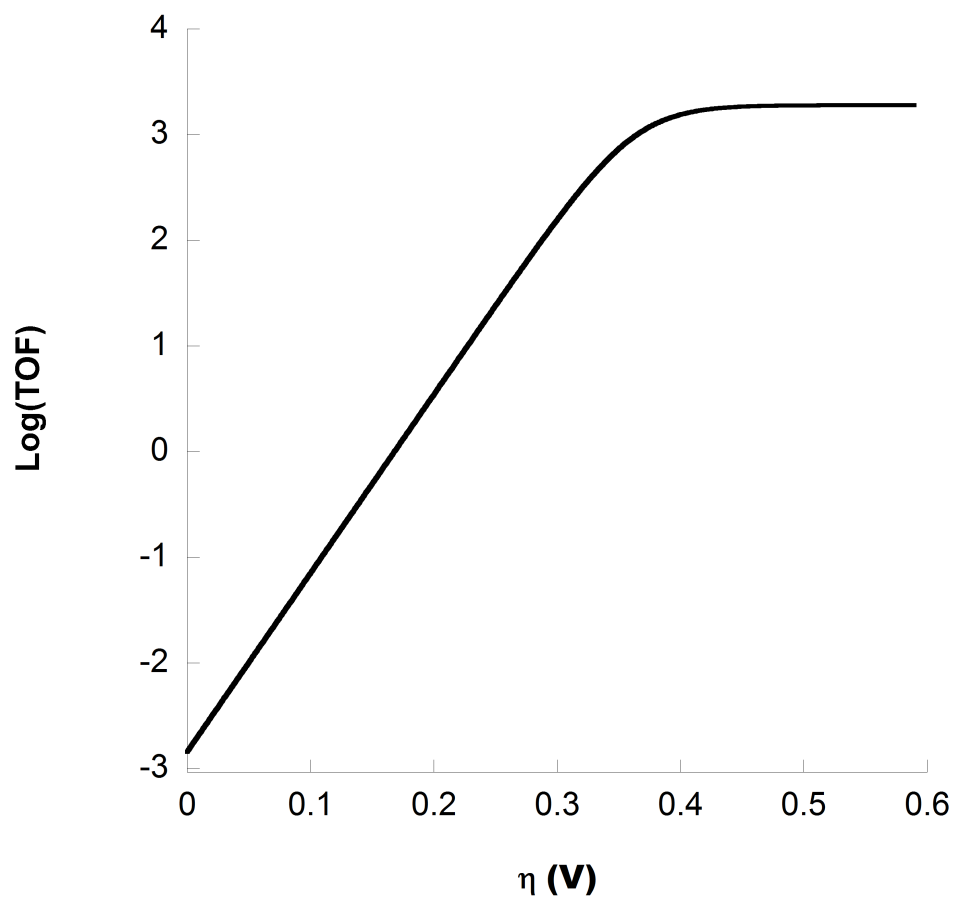


**Figure A9.** Tafel plot of **2** at  $v = 200 \text{ mV/s.}^2$

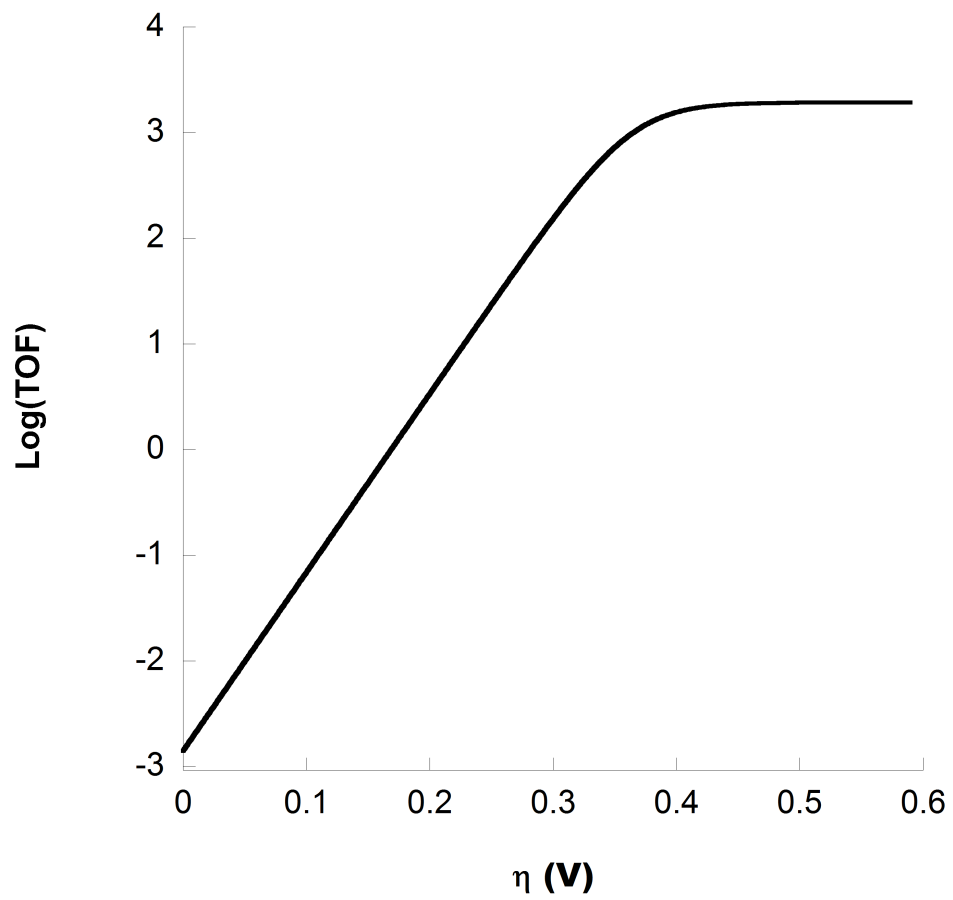


**Figure A10.** Tafel plot of **2** at  $v = 500 \text{ mV/s.}^2$

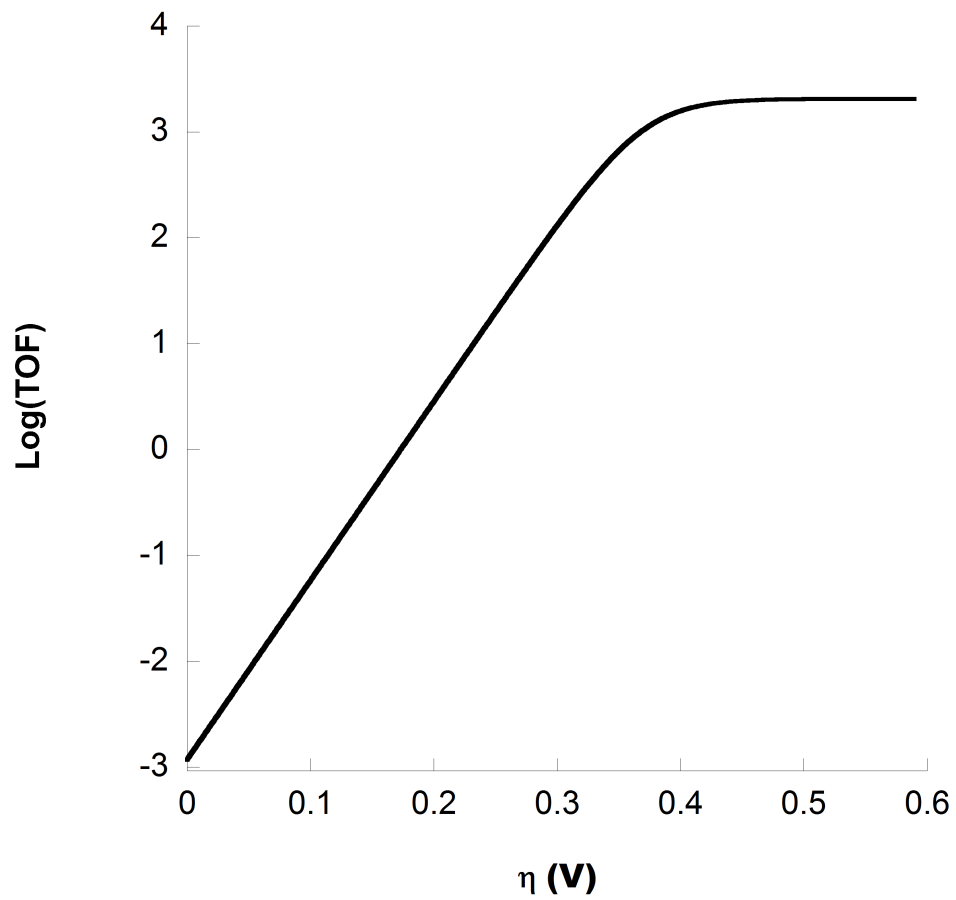


**Figure A11.** Tafel plot of **2** at  $v = 1 \text{ V/s.}^2$

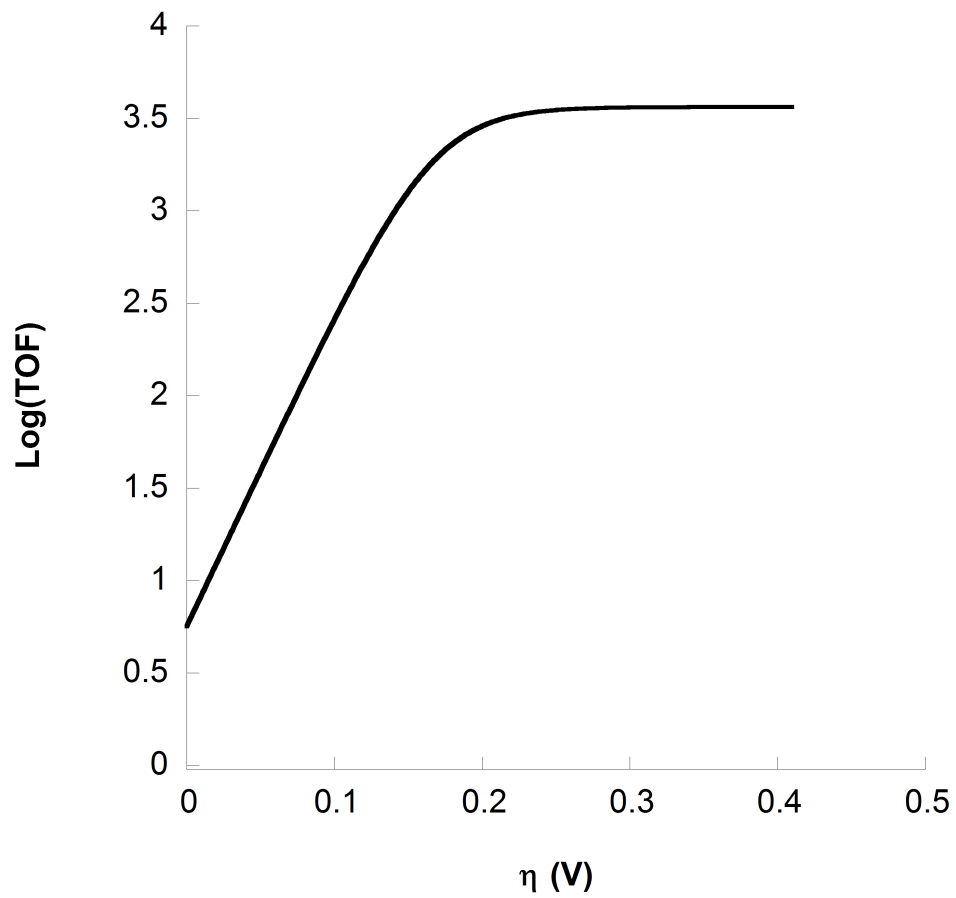


**Figure A13.** Tafel plot of 3 at  $v = 200 \text{ mV/s.}^2$



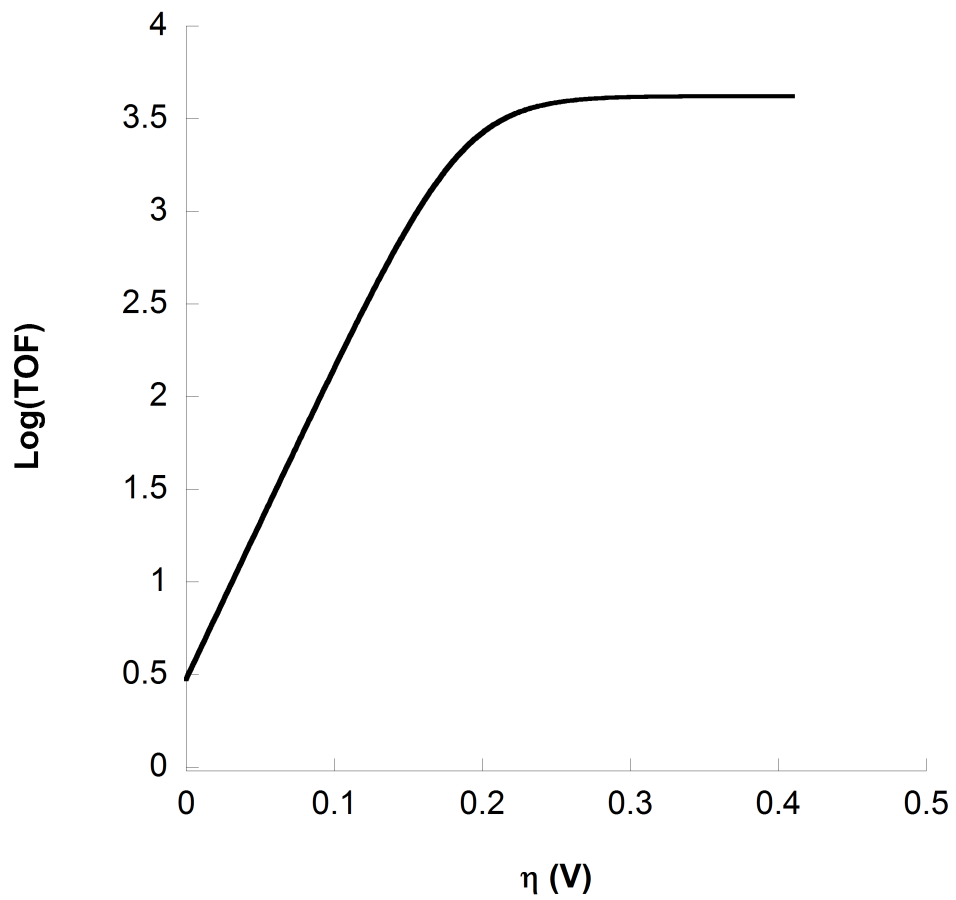


**Figure A14.** Tafel plot of 3 at  $v = 600 \text{ mV/s.}^2$

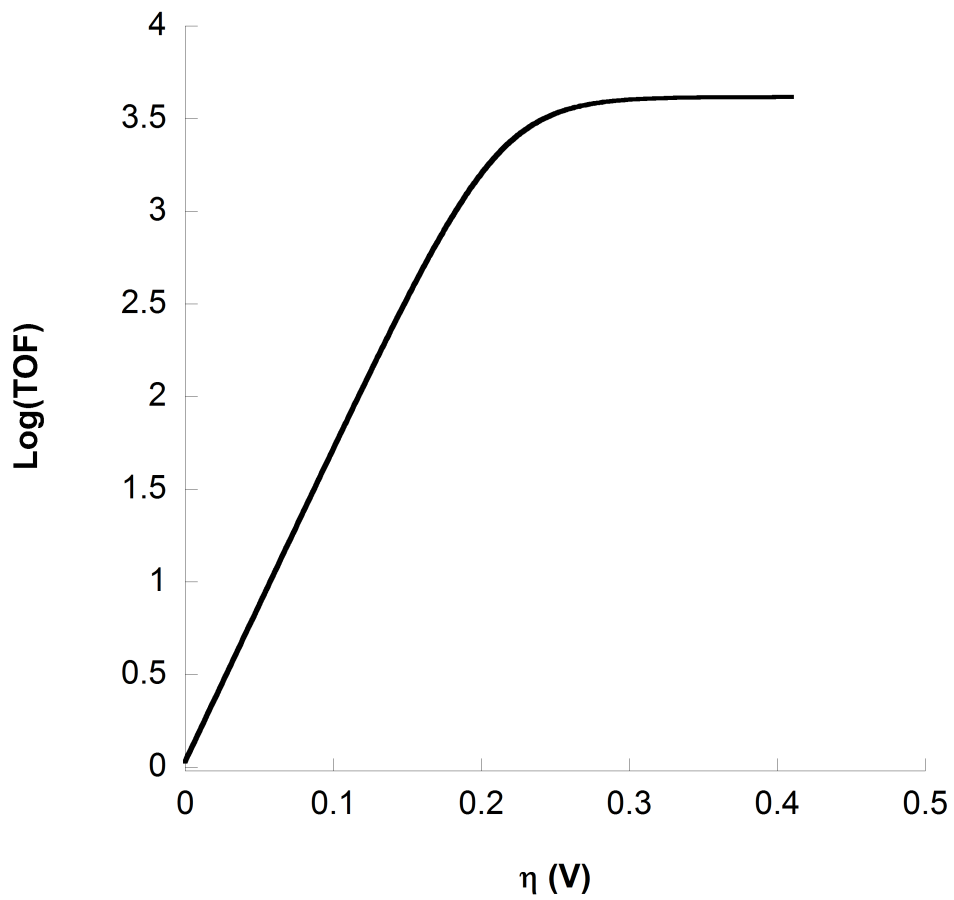


**Figure A15.** Tafel plot of **3** at  $v = 1 \text{ V/s.}^2$

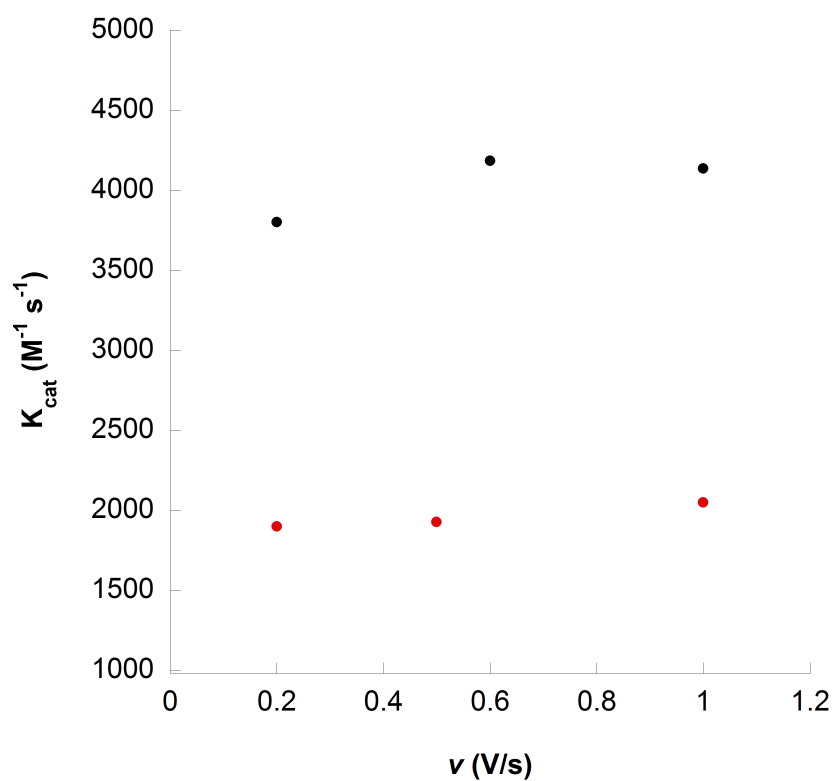


**Figure A16.**  $k_{\text{cat}}$  values for **2** (black) and **3** (red) at different scan rates. For complex **2** and **3**,  $k_{\text{cat}}$  levels off between  $v = 600$  mV/s and 1 V/s. Values for  $k_{\text{cat}}$  are equal to  $\text{TOF}_{\text{max}}$ .<sup>2</sup>

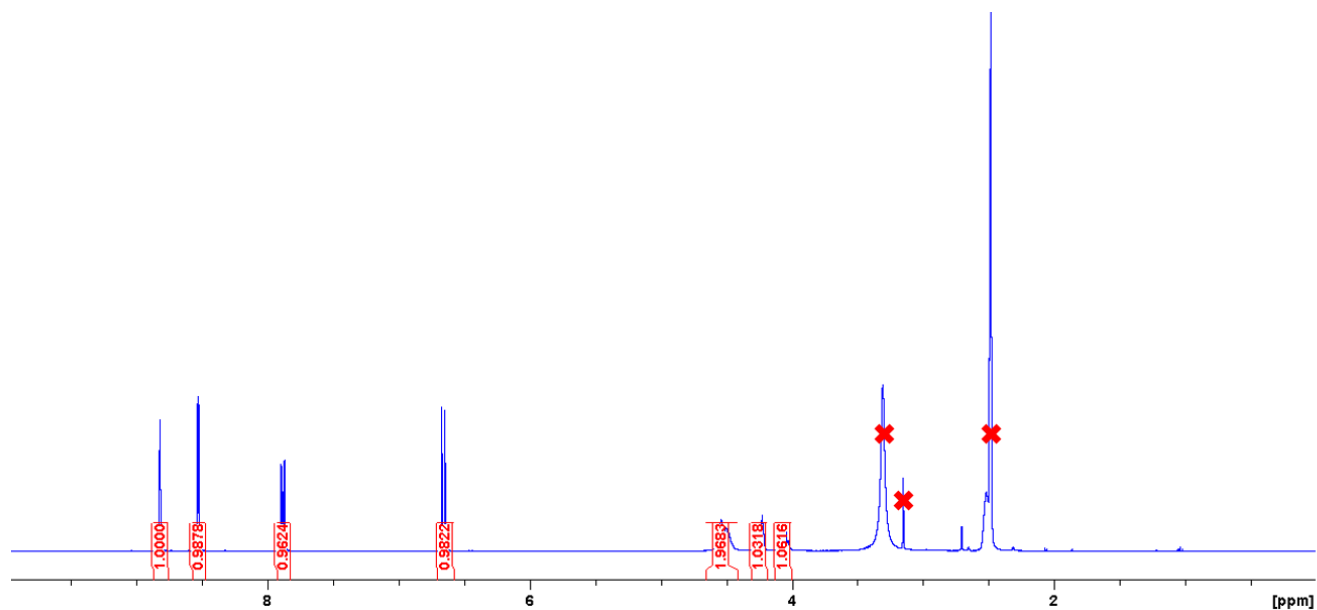


**Figure A17.**  $^1\text{H}$  NMR of **2** with integrations. Solvent impurities of water (3.31 ppm), methanol (3.16 ppm), and DMSO (2.48 ppm) are marked with x.<sup>2</sup>

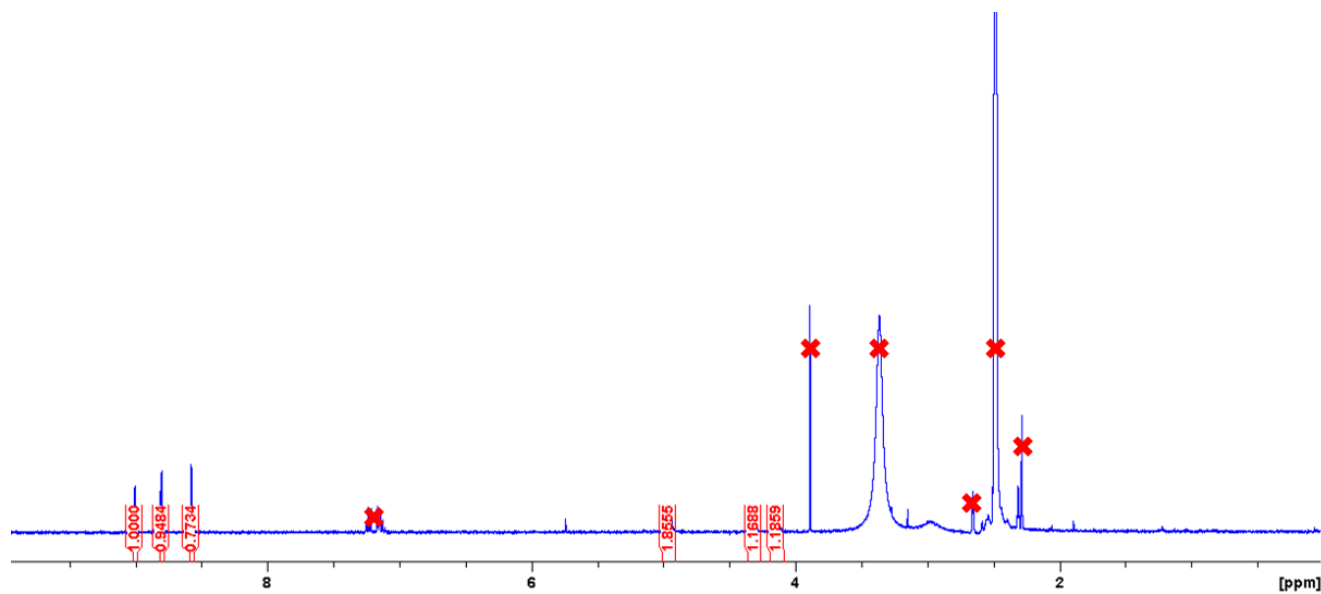


**Figure A17.**  $^1\text{H}$  NMR of **3** with integrations. Solvent impurities of toluene (7.2 ppm, 2.29 ppm), methanol (3.89 ppm), water (3.36 ppm), and DMSO (2.48 ppm) are marked with x.<sup>2</sup>

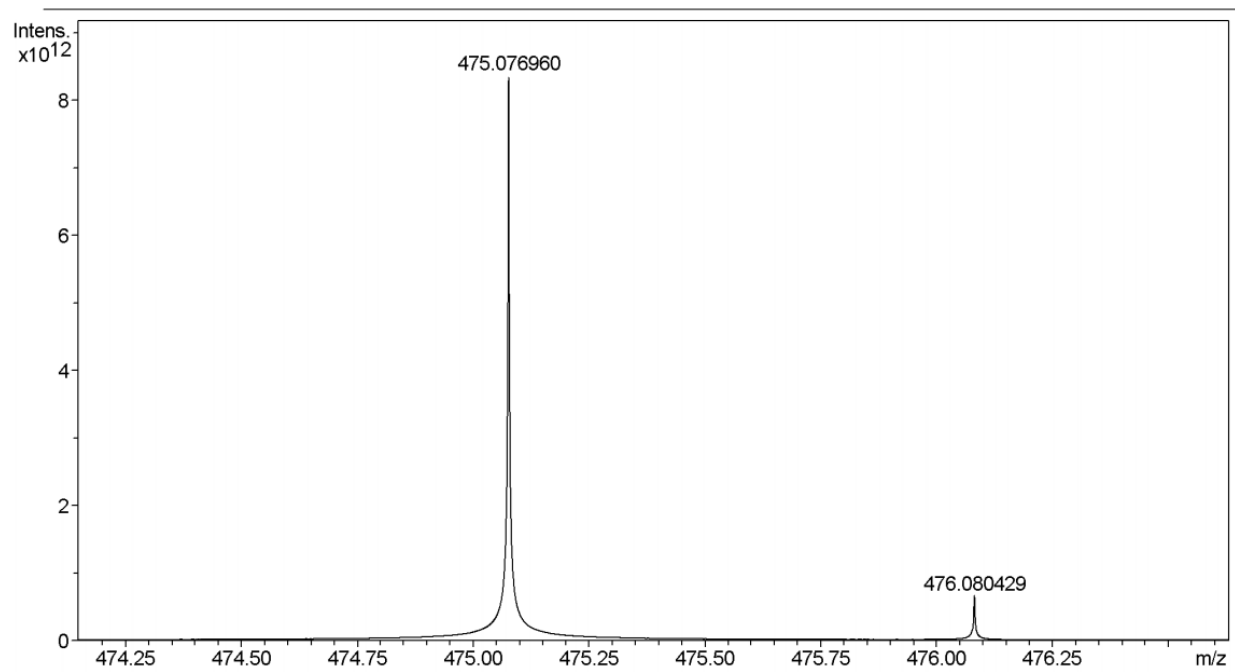


**Figure A18.** High-resolution mass spectrum of **2.2**

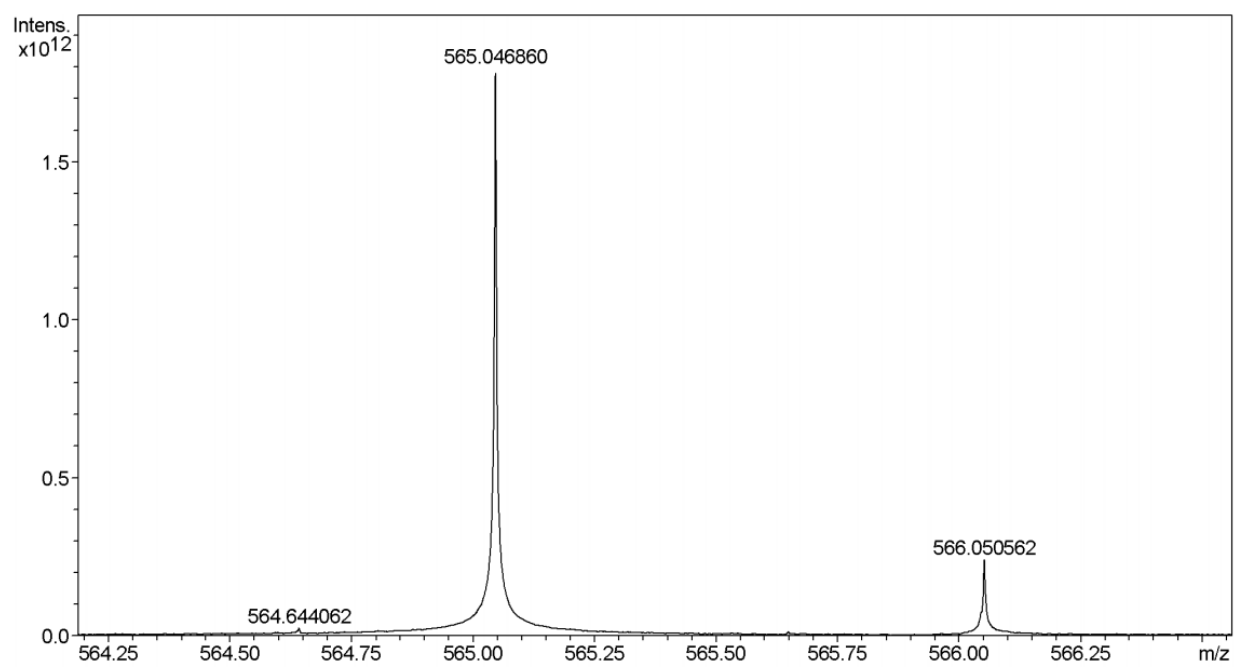


**Figure A18.** High-resolution mass spectrum of **3.2**

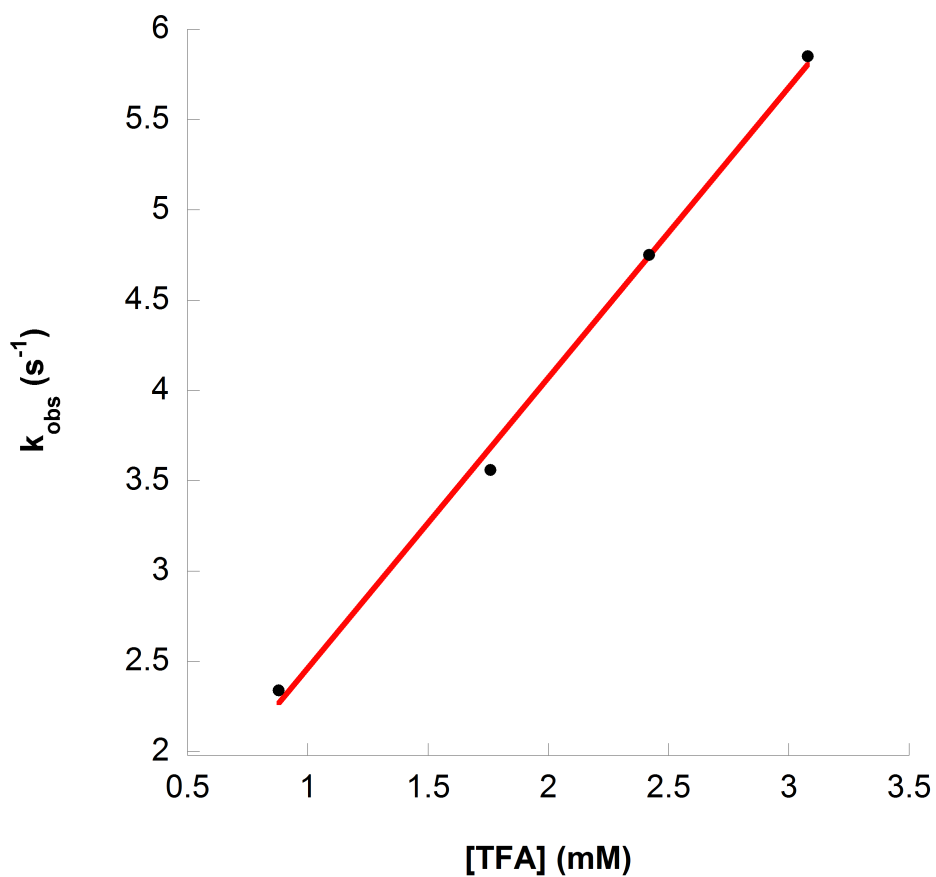


**Figure A19.** The  $k_{obs}$  vs.  $[H^+]$  for CVs of 0.5 mg of **2** in  $CH_3CN$  with 0.1 M  $TBAPF_6$  upon addition of 0.88 mM, 1.76 mM, 2.42 mM, and 3.08 mM TFA at  $v = 200$  mV/s.  $R^2 = 0.99$ .<sup>2</sup>

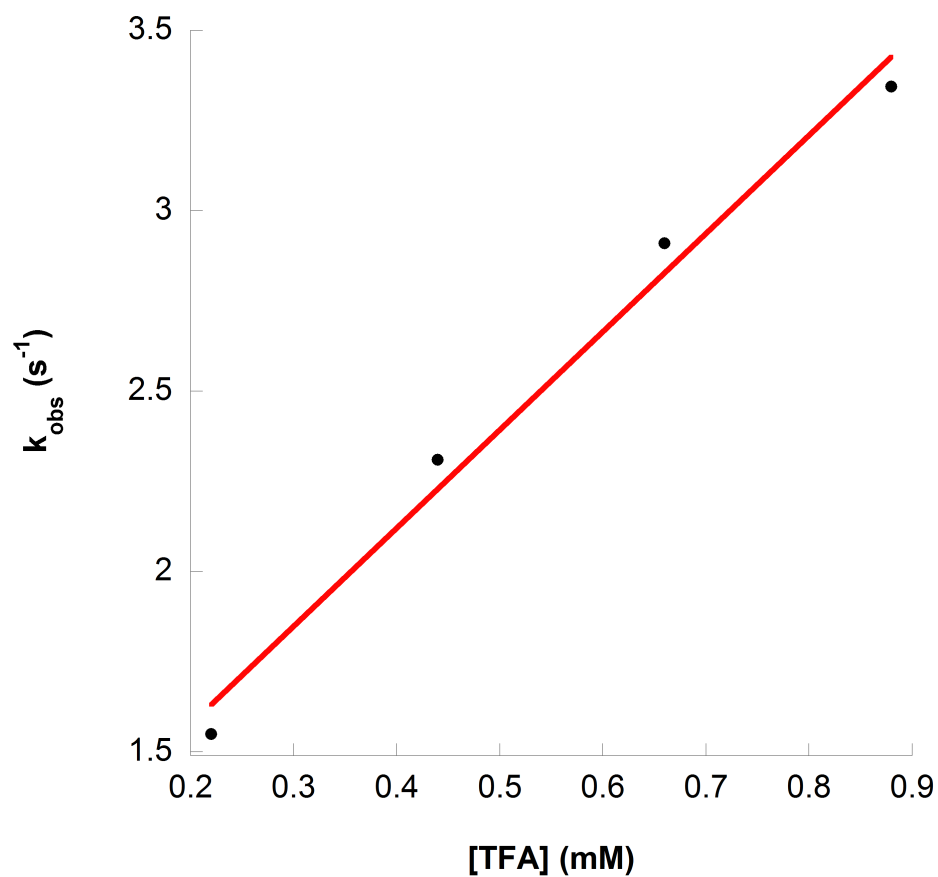


**Figure A20.** The  $k_{obs}$  vs.  $[H^+]$  for CVs of 0.5 mg of **3** in  $CH_3CN$  with 0.1 M  $TBAPF_6$  upon addition of 0.22 mM, 0.44 mM, 0.66 mM, and 0.88 mM TFA at  $v = 200$  mV/s.  $R^2 = 0.99$ .<sup>2</sup>

### Chapter 3: Exploration of Catalysts for the Oxygen Reduction Reaction Introduction

In addition to proton reduction, the Oxygen Reduction Reactions (ORR, **13-15**) have potential

$O_2 + 4H^+ + 4e^- \rightarrow 2H_2O$	<b>13</b>
$O_2 + 2H^+ + 2e^- \rightarrow H_2O_2$	<b>14</b>
$H_2O_2 + H_2 + 2e^- \rightarrow 2H_2O$	<b>15</b>

energy technology applications. For hydrogen fuel cells, (figure **1.4**) the cathodic reaction is either the four electron (equation **13**, right) or the two electron (equation **14**, right) pathways. Hydrogen fuel cells currently use an expensive Pt- or Pd-based catalyst,<sup>1,2</sup> so identification and development of inexpensive earth abundant metal catalysts would reduce the cost of such system and lead to their implementation. Current common earth metal catalysts for ORR are almost all biologically inspired heme macrocycles.<sup>1</sup> It is of interest to develop non-heme systems for ORR. Variety in choice of electrocatalyst allows for a greater range of solubilities, as previously reported heme systems have had limited solubility in water.<sup>1b</sup> Additionally, these provide a basis for searching for non-heme derived catalysts that may be superior. Finally, having a choice of catalysts improves the ability to construct heterogeneous systems.

When evaluating electrocatalysts for ORR, activity and efficiency can be measured using similar techniques and metrics as proton reduction. Foot of the wave analysis extracts rate constants and TOFs for ORR from cyclic voltammetry (CV), and overpotential is calculated the same way (see equations **5-7, 9**). However, unlike proton reduction, there are two primary reactions for ORR, **13** and **14**. It is critical to determine selectivity of a catalyst before calculations, as both FOWA and overpotential calculations vary with selectivity. Note that it is common for a catalyst to reduce  $O_2$  by a mixture of both pathways.<sup>1</sup>



For a hydrogen fuel cell, the four-electron pathway is the desirable one. As fuel cells exhaust the product into the atmosphere, control of the product is key to keep the harm to the environment low. Equation **13** is superior because it releases water and not hydrogen peroxide into the atmosphere as a byproduct.<sup>1</sup> Additionally, the energy of the electrons produced in the fuel cell is dependent on the difference in standard reduction potentials for the ORR pathway and hydrogen evolution. For equation **13**, the standard aqueous reduction potential is 1.229 V vs SHE, while **14** is 0.695 V vs SHE. This indicates that **13** is thermodynamically favored. However, equation **14** only requires five substrates, compared to the nine required for **13**, so **14** is kinetically favored. Catalysts that are selective for **14** are also useful in hydrogen peroxide fuel cells, which function similarly to hydrogen fuel cells but use H<sub>2</sub>O<sub>2</sub> at the anode instead of H<sub>2</sub>. In practice, an important additional pathway is the 2+2 mechanism, and it is the reactions **14** and **15** (the reduction of H<sub>2</sub>O<sub>2</sub>) sequentially.<sup>3</sup> This pathway is generally less used,<sup>1,3</sup> but it is important to account for it in experiments.

Regardless of mechanism, intermediates for ORR are well known.<sup>1,3</sup> An important possible intermediate is O<sub>2</sub><sup>-•</sup>, the dioxygen radical.<sup>1</sup> Since this intermediate and other similar reactive oxygen species are common, they can cause major problems such as catalyst decomposition and may react with other parts of the solution. This is a major cause of high overpotential and inefficiency in ORR systems.<sup>1</sup>

Reaction selectivity is determined by Rotating-Ring Disk Voltammetry (RRDV). In RRDV there are four electrodes: a rotating ring electrode and disk electrode, a counter electrode, and a reference electrode. The counter and reference electrodes are the same as in CV, but the ring and disk electrodes both induce current in solution independent of one

another. Usually, the ring potential is constant and the disk potential sweeps (like a CV).<sup>9</sup> Additionally, the ring and disk both rotate at a fixed rate.

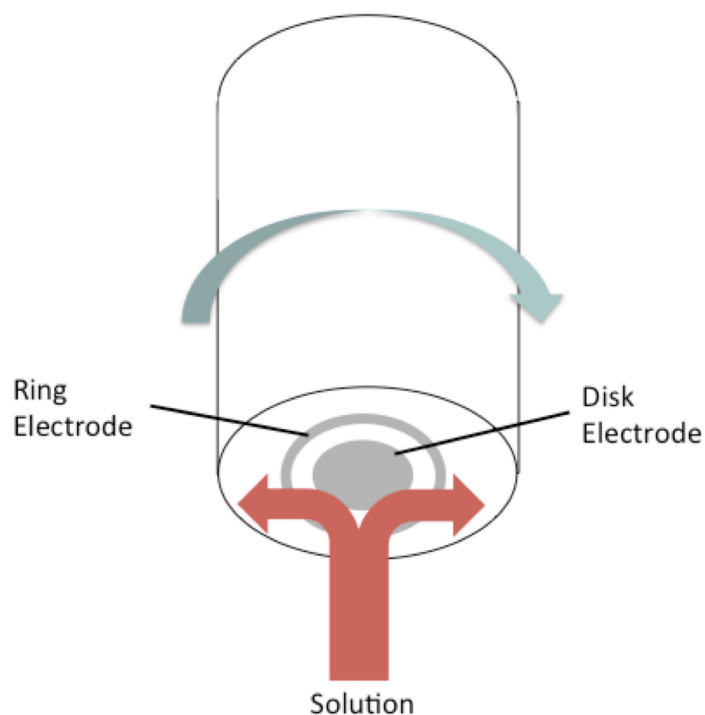


**Figure 3.1.** Diagram of a Rotating Ring Disk Electrode setup.

Measured current at the disk electrode is assumed to be primarily the catalyzed reaction.<sup>10</sup> Equation **15** has been observed at the disk, but it is sufficiently slow as to assume it does not happen on the time scale of the experiment.<sup>10</sup> After the disk reaction occurs, the flow of solvent pushes the product away from the disk and to the ring electrode as seen in figure **3.1**. Any  $\text{H}_2\text{O}_2$  in the product is reduced to  $\text{H}_2\text{O}$  at the ring, and ring current thus corresponds primarily to equation **15**. We hold the ring current fixed at a high potential (+600 mV vs  $\text{Fc}^+/\text{Fc}$ ), because neither equation **13** nor **14** have been observed at that high of a potential for any of our catalysts.

Then the selectivity is determined from the ratio of current at the disk and ring electrodes by equation **16**.<sup>10,11</sup>

$$\%H_2O_2 = \frac{100 \left( \frac{2i_{ring}}{N} \right)}{i_{disk} + \frac{i_{ring}}{N}}, \quad 16$$

where  $i_{ring}$  is the current at the ring, and  $i_{disk}$  is the current at the disk.  $N$  is the collection efficiency, which is a property of the specific instrument. The result,  $\%H_2O_2$ , gives the relative amount of  $O_2$  reduced via equation **14**.

After selectivity is determined, kinetic analysis follows. FOWA presented in Chapter 1 can be used to extract rate constants from non-ideal CV scans of the catalyst in an acid-addition study. The major difference is that the formula for  $i_c$  must account for a different number of electrons depending on the ORR selectivity.

Overpotential calculation is similar to proton reduction as well; equation **6** still is the primary method of overpotential calculation. Unfortunately, thermodynamic potential has not been experimentally tabulated for all solvent/acid pairs under both 2 and 4 electron mechanisms. Instead, using the Nernst equation, **17** gives  $E_{therm}$  in aqueous solvents, and equation **18** adjusts for non-aqueous solvents<sup>1,3</sup>. For a non-aqueous solvent, a buffered solution is necessary because of equilibrium considerations, since  $[A^-]$  increases as the reaction proceeds and will affect equilibrium potentials<sup>1</sup>.

$$E_{therm} = E^o - \frac{RT}{nF} \ln Q \quad 17$$

$$E_{therm} = E^o - \frac{RT}{nF} \ln Q - 0.0592pK_a \quad 18$$

$$Q = \frac{[H_2O]^2 [A^-]^4}{P_{O_2} [HA]^4} \quad 19$$

Where thermodynamic potential under standard conditions is  $E^0$ , and  $Q$  is the equilibrium quotient, seen in equation **19**.<sup>1,3</sup> Again, note that  $E^0$  depends greatly on mechanism, so selectivity of the catalyst matters greatly.

Very few catalyst designs have been known to successfully reduce oxygen.<sup>2</sup> The most successful homogeneous catalysts have been heme-derived, but literature examining the ability of non-heme catalysts is much rarer.<sup>2</sup> We evaluated non-heme catalysts for their ability to reduce oxygen, and compared with the simplest heme standard, **1**. Compounds are shown in Figure **3.1**.

Herein, we report results in qualitative identification of proton reduction catalysts that are also active for ORR. Kinetic studies have not yet been performed, but several promising candidates have been identified. All catalysts were compared to a blank CV with the absence of catalyst, and active catalysts were identified by current enhancement over the control run. For a selected catalyst, **5**, RRDV was employed to determine selectivity of the catalyst.

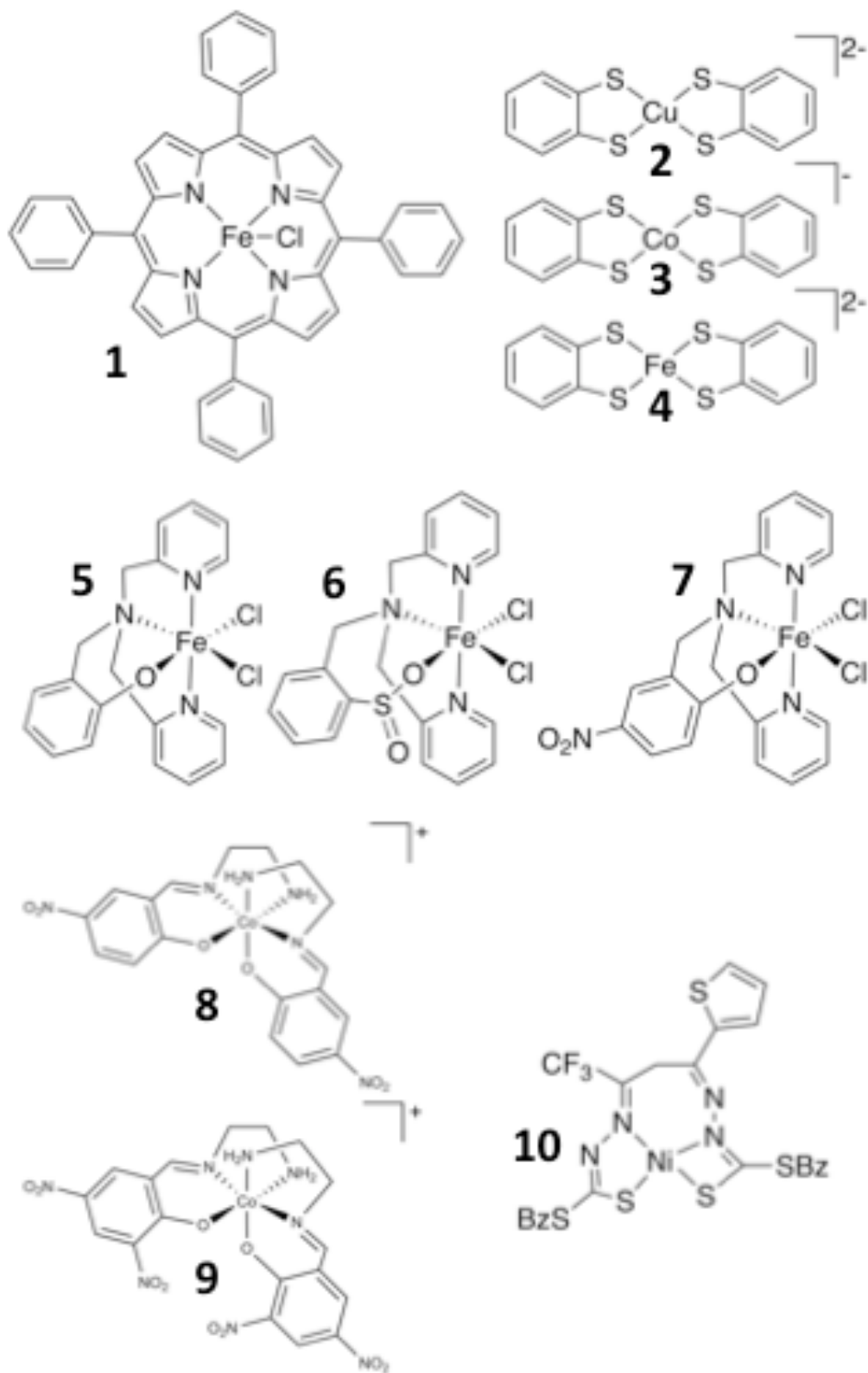


**Figure 3.2.** Proton reduction catalysts **2-10** investigated for ORR activity, and control catalyst **1**.<sup>4-9</sup>

## **Experimental Methods**

### **Materials**

All reagents were purchased from Aldrich and used without further purification unless otherwise mentioned. Complex **1** was purchased from Fisher Scientific and used without further purification.

### **Methods.**

**Synthesis of 2.** Compound **2** was synthesized using a modified literature procedure.<sup>5</sup>

**Synthesis of 3.** 289.5 mg (0.45 mmol) of Co(Bf<sub>4</sub>) hexahydrate was combined with 384.5 mg (1.8 mmol) KO<sup>t</sup>Bu in 30 mL MeOH and allowed to stir under Ar at room temperature for 30 min. 237.1 mg (1.1 mmol) 1,2-benzenedithiol was degassed in MeOH then added to the Co solution. The resulting solution was stirred for 4 hours at room temperature, then 275.2 mg (0.85 mmol) TBABr was added and stirred overnight. The solution was evaporated under reduced pressure and a dark blue precipitate formed. It was dissolved in the minimum amount of DCM necessary then layered over diethylether. Compound **3** (a blue crystalline solid) crystallized from the mixture after 12 hours and used without further purification or characterization.<sup>5</sup>

**Synthesis of 4.** Compound **4** was synthesized using a modified literature procedure.<sup>5</sup>

**Synthesis of 5.** Compound **5** was synthesized according to literature procedure.<sup>6</sup>

**Synthesis of 6.** Compound **6** was synthesized according to literature procedure.<sup>7</sup>

**Synthesis of 7.** Compound **7** was synthesized according to literature procedure.<sup>8</sup>

**Synthesis of 8.** Synthesis of **8** is included in Chapter **1, Experimental methods.**

**Synthesis of 9.** Synthesis of **9** is included in Chapter **1, Experimental methods.**

**Synthesis of 10.** Compound 7 was synthesized according to literature procedure.<sup>9</sup>

### **Cyclic Voltammetry**

Experiments were performed with either a CH Instruments 620D potentiostat or a CH Instruments 680E bipotentiostat in CV mode. Unless otherwise noted, experiments were performed with a vitreous carbon working electrode (radius 1.5 mm) and a Pt auxiliary electrode. Electrodes were polished between scans with 0.05  $\mu\text{m}$  alumina/water paste on a cloth covered tile, then rinsed with water and further polished with a solvent-soaked paper towel and rinsed with solvent. Scans were carried out against a SCE or Ag/AgCl reference electrode and ferrocene was used as an internal standard against reference electrode drift. All potentials listed here are against the  $\text{Fc}^+/\text{Fc}$  couple unless otherwise indicated. All experiments used an Ar balloon for initial background then an  $\text{O}_2$  balloon to establish an  $\text{O}_2$  atmosphere. Unless otherwise noted, added acid was the triflic salt of DMF ([HDMF]Otf). Other commonly used salts were paired with solvents according to literature procedures<sup>1,3</sup>. The common pairs were MeCN and [HDMF]Otf, MeOH and  $\text{CH}_3\text{COOH}$ , and DMF and  $\text{HClO}_4$ .

### **Acid Addition**

Cyclic Voltammograms were obtained using 0.5 mg of crystal in 5.0 mL MeCN and 0.1 M TBAPF<sub>6</sub>. CVs were obtained at 25° C, at various scan rates and concentrations of acid. All studies included a background scan with no TFA in an Ar atmosphere.

### **Rotating Ring Disk Voltammetry**

Experiments were performed with a CH Instruments 750E bipotentiostat doing linear sweep voltammetry. Experiments were performed with a Pt disk/Pt ring so as to eliminate any possibility of a ring/disk cross contamination during polishing. Polishing of

the ring and disk was done by 1  $\mu\text{m}$  diamond/water paste on a Buehler polishing pad. They were then rinsed with solvent to remove any particles. The reference electrode was an Ag/AgCl electrode, and the counter electrode was a Pt wire. The counter electrode was thoroughly sanded prior to each experiment to remove any buildup between experiments. Experiments were carried out in a shot glass, using 15 mL or 20 mL of solution depending on the specific piece of glassware. Glasses were rinsed with sulfuric acid, water, and acetone between experiments. Experiments were done in the absence of ferrocene.

### **Collection Efficiency**

Collection Efficiency,  $N$ , of our RRDV setup was determined according to literature procedure.<sup>10,11</sup> A Pt ring/Pt disk working electrode pair was submerged in a solution of 0.1 M  $\text{K}_3\text{Fe}(\text{CN})_6$  and 0.1 M KCl in water. The solution was degassed with Ar for 10 minutes, then run at  $\omega = 400, 900, 1600, \text{ and } 2500$  rpm. The plateau current for the ring over the plateau current of the disk was averaged and found to be 39.2%. Theoretical collection efficiency is 42%.



## Results and Discussion

Compounds **1-10** were investigated for oxygen reduction using CV. A catalytic feature was determined to be current enhancement over the absence of catalyst. In addition to compound **1**, compounds **3, 4, 5**, and **6** were found to show current enhancement over the absence of catalyst. All other compounds show current decrease compared to the absence of catalyst, indicating meaningful presence of side reactions like proton reduction.

Compound **5** was selected for further selectivity study using RRDV. The ring and disk currents revealed the percent selectivity for the two electron pathway to be 8.5%. This value is an average of the selectivity at the half wave potential and at  $\pm 50$  mV. This indicates that for future studies, we can treat compound **5** as selective for the four electron pathway **13**.<sup>1</sup>

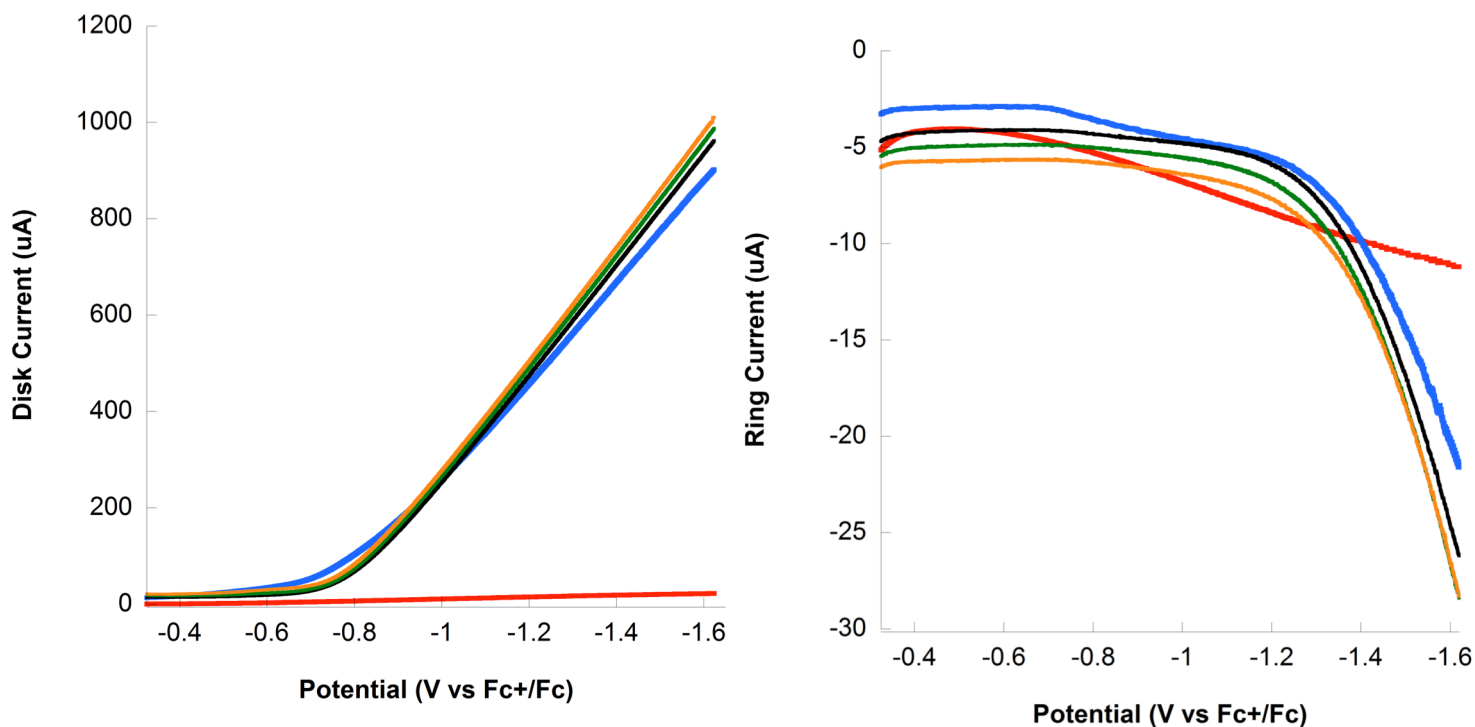


**Figure 3.3.** Disk and ring currents for RRDV on **5** and 0.1 M TBAPF<sub>6</sub> in DMF. All runs were in a 1 atm O<sub>2</sub> atmosphere. Rotation speeds are 400 rpm (red), 400 rpm (blue), 900 rpm (black) 1600 rpm (green) and 2500 rpm (orange). The red was performed in absence of acid, all others included 20 mM HDMFOTf.

We report nine compounds previously synthesized for proton reduction that were tested for oxygen reduction reaction activity. Four of the nine compounds tested were found to be active, as determined by qualitative comparison with known ORR catalyst **1** and catalyst free baselines under acid addition studies. We note that ORR mechanism has only been determined for catalyst **5**, and as such complete quantitative studies cannot be completed at this time. Future work on the project includes complete characterization of the selectivity for each of the active catalysts and quantitative study of the kinetic information and overpotential. In addition, the methods tested in this preliminary search for electrocatalysts may be used to find other catalysts for ORR.

## References

1. (a) M. L. Pegis, C. F. Wise, D. J. Martin, and J. M. Mayer, *Chem. Rev.*, **2018**, 18 (5), 2340–2391. (b) M. L. Pegis, B. A. McKeown, N. Kumar, K. Lang, D. J. Wasylenko, X. P. Zhang, S. Raugai and J. M. Mayer. *ACS Cent. Sci.* **2016**, 2 (11), 850–856.
2. S. Fukuzumi, Y. Lee, W. Nam., *Chem Cat Chem*, **2018**, 10 (9).
3. A. C. McQuilken, Y. Jiang, Maxime A. Siegler, and D. P. Goldberg, *J. Am. Chem. Soc.* **2012**, 134(21), 8758-8761
4. R. J. DiRisio, J. E. Armstrong, M. A. Frank, W. R. Lake and W. R. McNamara *Dalton Trans.*, 2017, 46, 10418-10425
5. (a) W. R. McNamara, Z. Han, P. J. Alperin, W. W. Brennessel, P. L. Holland, and R. Eisenberg. *J. Am. Chem. Soc.* **2011**, 133 (39), 15368–15371. (b) D. Sellmann, M. Geck, M. Moll. *J. Am. Chem. Soc.* **1991**, 113, 5259. (c) B. K. Maiti, et al. *Inorg. Chem.*, **2014**, 53 (24), 12799–12808. DOI: 10.1021/ic501742j
6. G. Connor, K. J. Mayer, C. S. Tribble, and W. R. McNamara. *Inorg. Chem.* **2014**, 53, 5408-5410.
7. A. C. Cavell, C. L. Hartley, D. Liu, C. S. Tribble, and W. R. McNamara. *Inorg. Chem.*, **2015**, 54 (7), 3325–3330
8. C. L. Hartley, R. DiRisio, T. Y. Chang, W. Zhang, and W. R. McNamara. " *Polyhedron*, **2016**, 114, 133-137.
9. C. F. Wise, D. Liu, K. J. Mayer, P. M. Crossland, C. L. Hartley and W. R. McNamara. *Dalton Trans.*, **2015**, 44, 14265-14271.
10. Z. Jia, G. Yin, J. Zhang. *Rotating Electrode Catalysts and Oxygen Reduction Catalysts*. **2014**. <https://doi.org/10.1016/B978-0-444-63278-4.00006-9>
11. Pine Instruments. *Rotating Electrode Theory*. From <https://www.pineresearch.com/shop/knowledgebase/pine-rotating-electrode-theory>.

## Appendix B

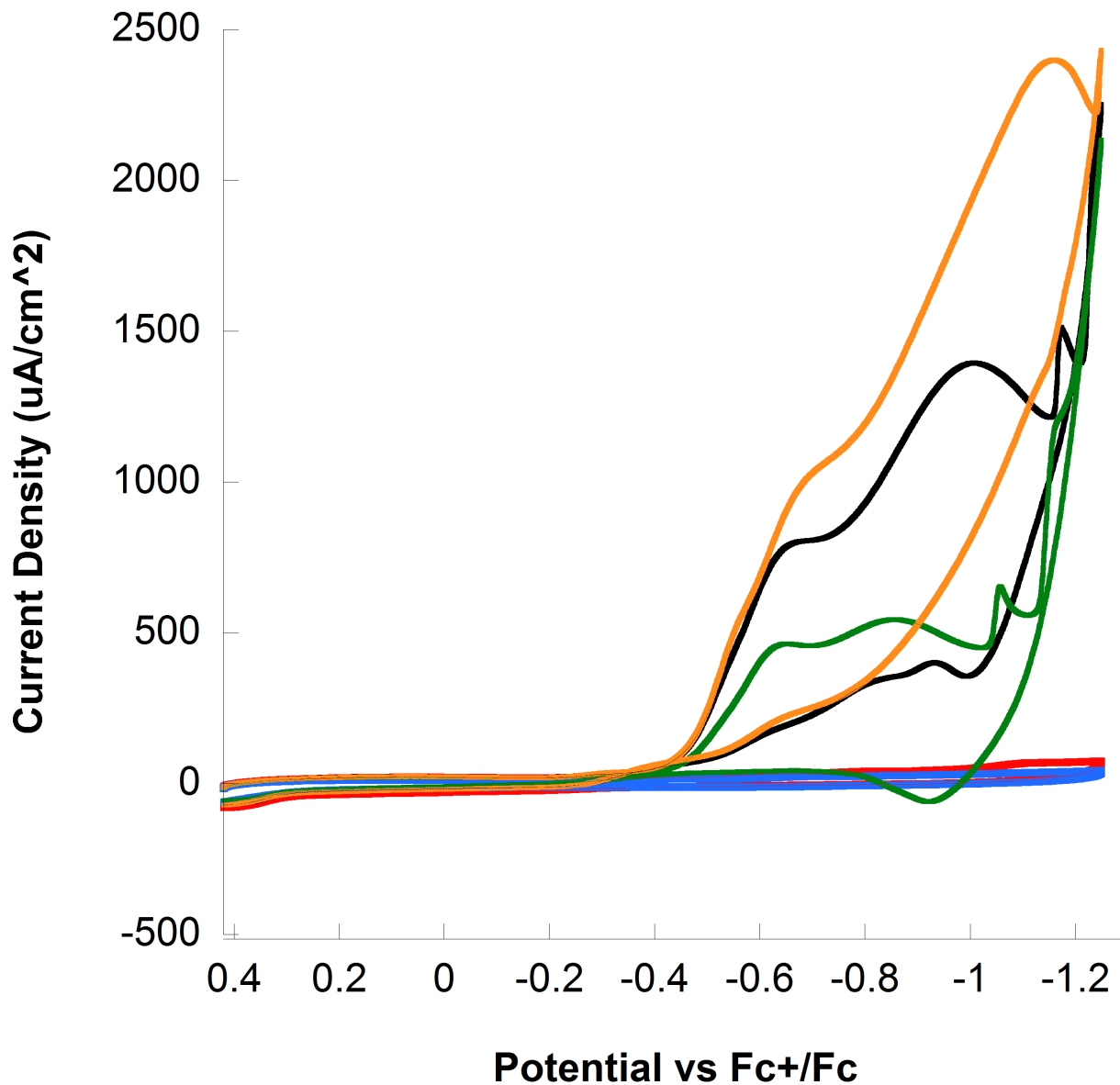


**Figure B1.** CV of **1** in MeCN with 0.1 M TBAPF<sub>6</sub>. Scans were with 0 mM HDMFOTf/Ar (blue), 3.5 mM HDMFOTf/Ar (red), 3.5 mM HDMFOTf/O<sub>2</sub> (green), 7 mM HDMFOTf/O<sub>2</sub> (black), 10.5 mM HDMFOTf/O<sub>2</sub>(orange). All gasses were at 1 atm.

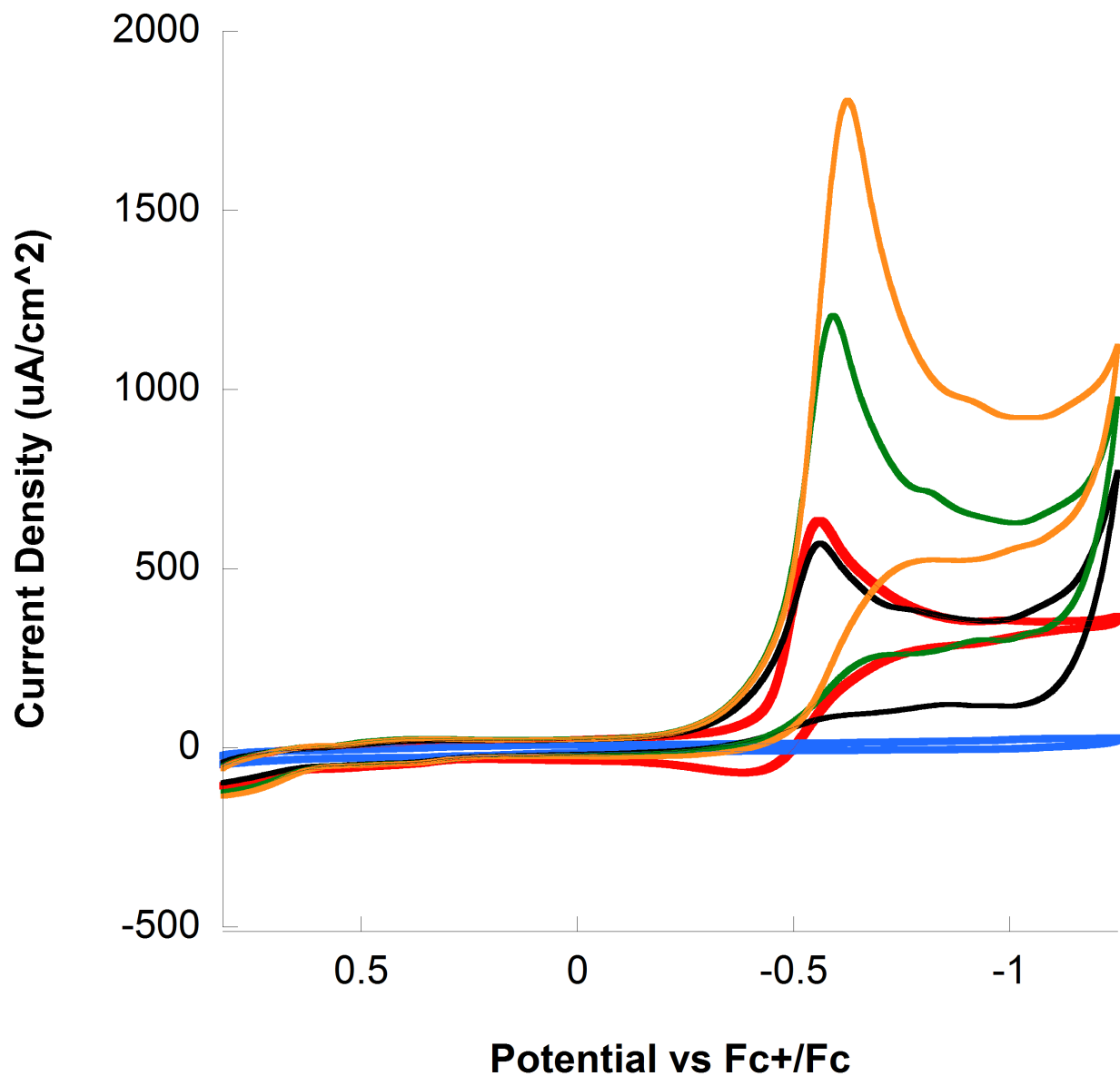


**Figure B2.** CV of **2** in MeCN with 0.1 M TBAPF<sub>6</sub>. Scans were with 0 mM HDMFOTf/Ar (blue), 3.5 mM HDMFOTf/Ar (red), 3.5 mM HDMFOTf/O<sub>2</sub> (black), 7 mM HDMFOTf/O<sub>2</sub> (green), 10.5 mM HDMFOTf/O<sub>2</sub>(orange). All gasses were at 1 atm. This used a Pt working electrode instead of vitreous carbon.

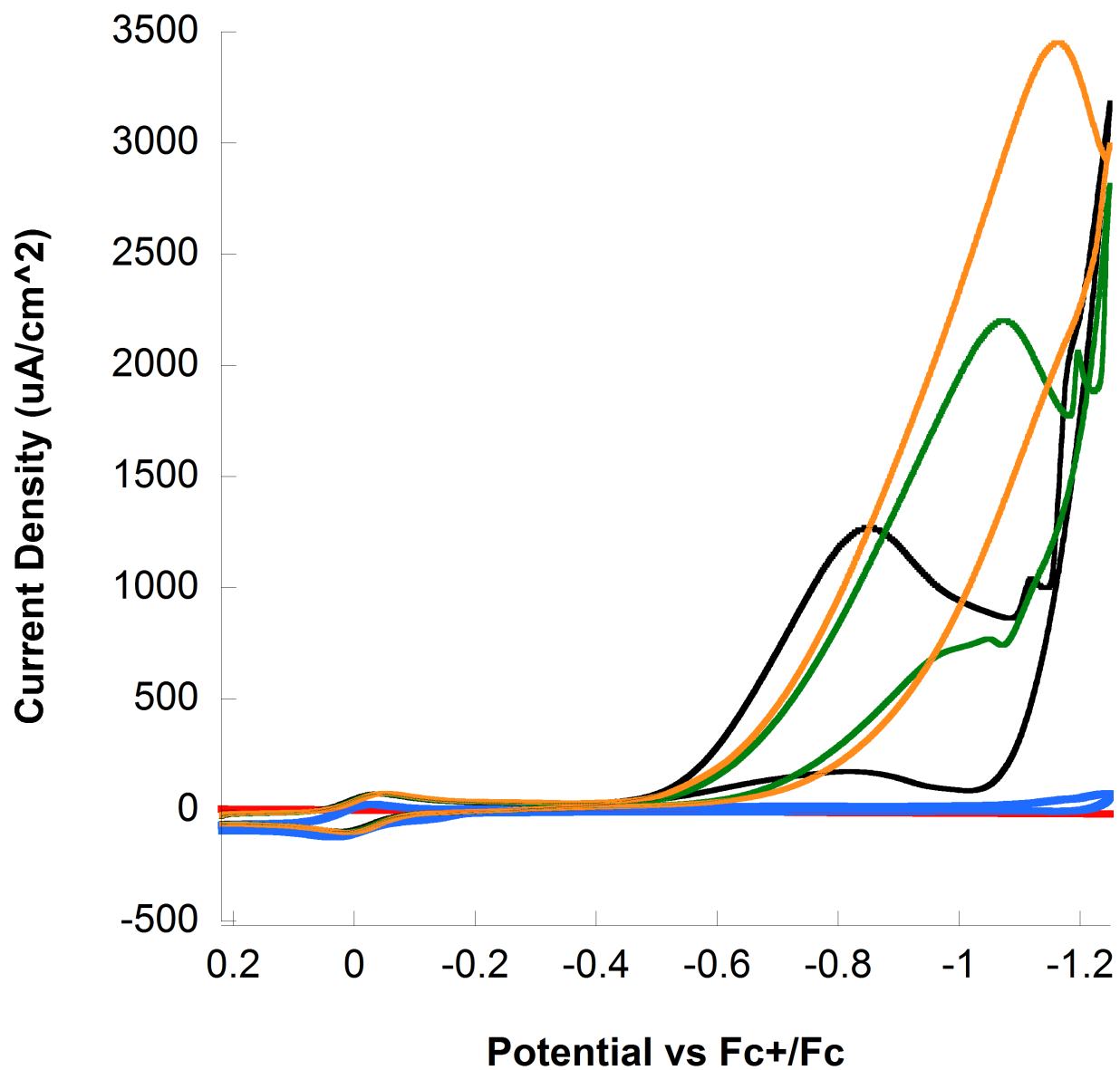


**Figure B3.** CV of **3** in MeCN with 0.1 M TBAPF<sub>6</sub>. Scans were with 0 mM HDMFOTf/Ar (red), 3.5 mM HDMFOTf/Ar (blue), 3.5 mM HDMFOTf/O<sub>2</sub> (black), 7 mM HDMFOTf/O<sub>2</sub> (green), 10.5 mM HDMFOTf/O<sub>2</sub> (orange). All gasses were at 1 atm.

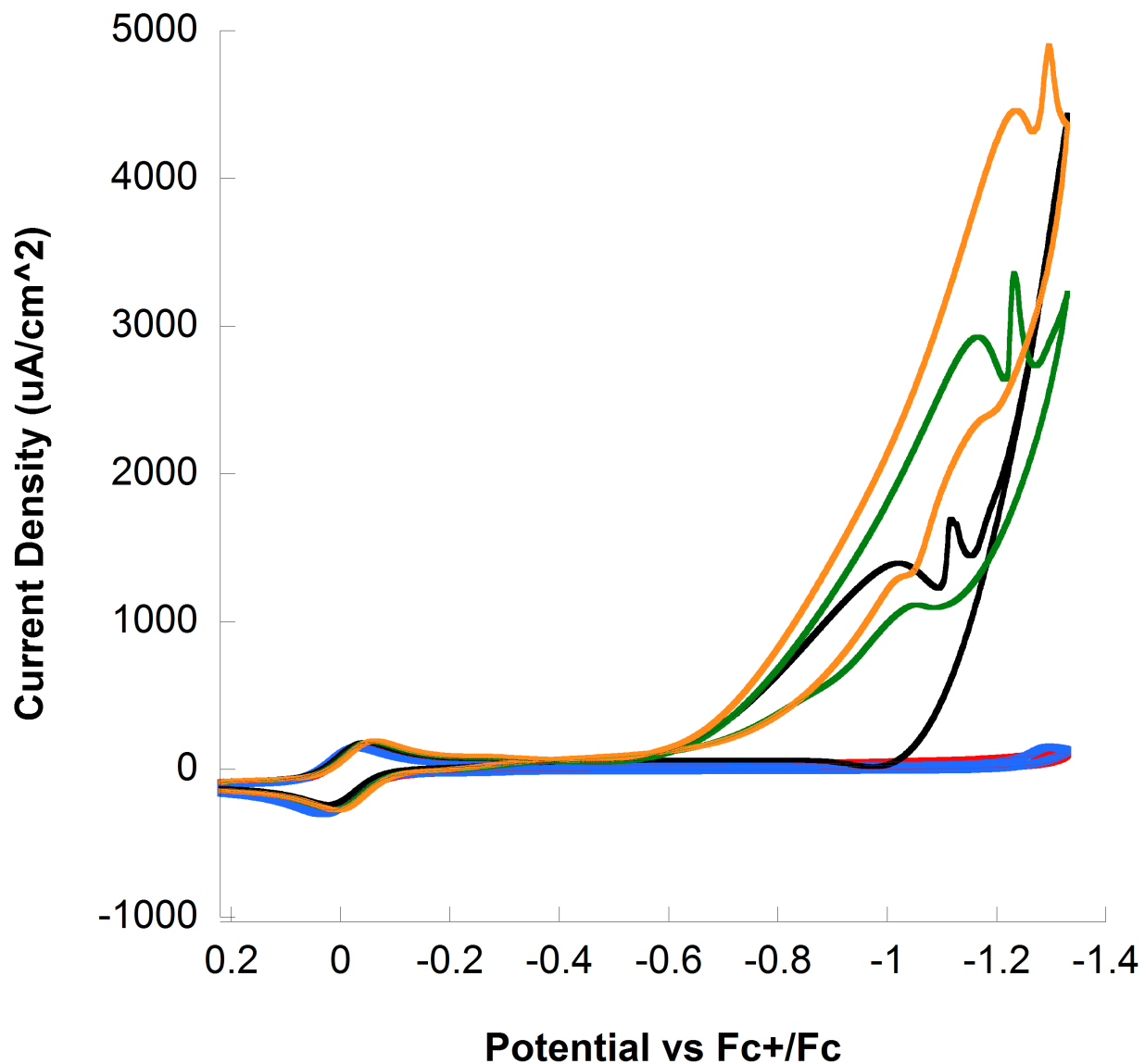


**Figure B4.** CV of **4** in MeCN with 0.1 M TBAPF<sub>6</sub> and a Fc<sup>+</sup>/Fc internal standard. Scans were with 0 mM HDMFOTf/Ar (red), 3.5 mM HDMFOTf/Ar (blue), 3.5 mM HDMFOTf/O<sub>2</sub> (green), 7 mM HDMFOTf/ O<sub>2</sub> (black), 10.5 mM HDMFOTf/O<sub>2</sub> (orange). All gasses were at 1 atm.

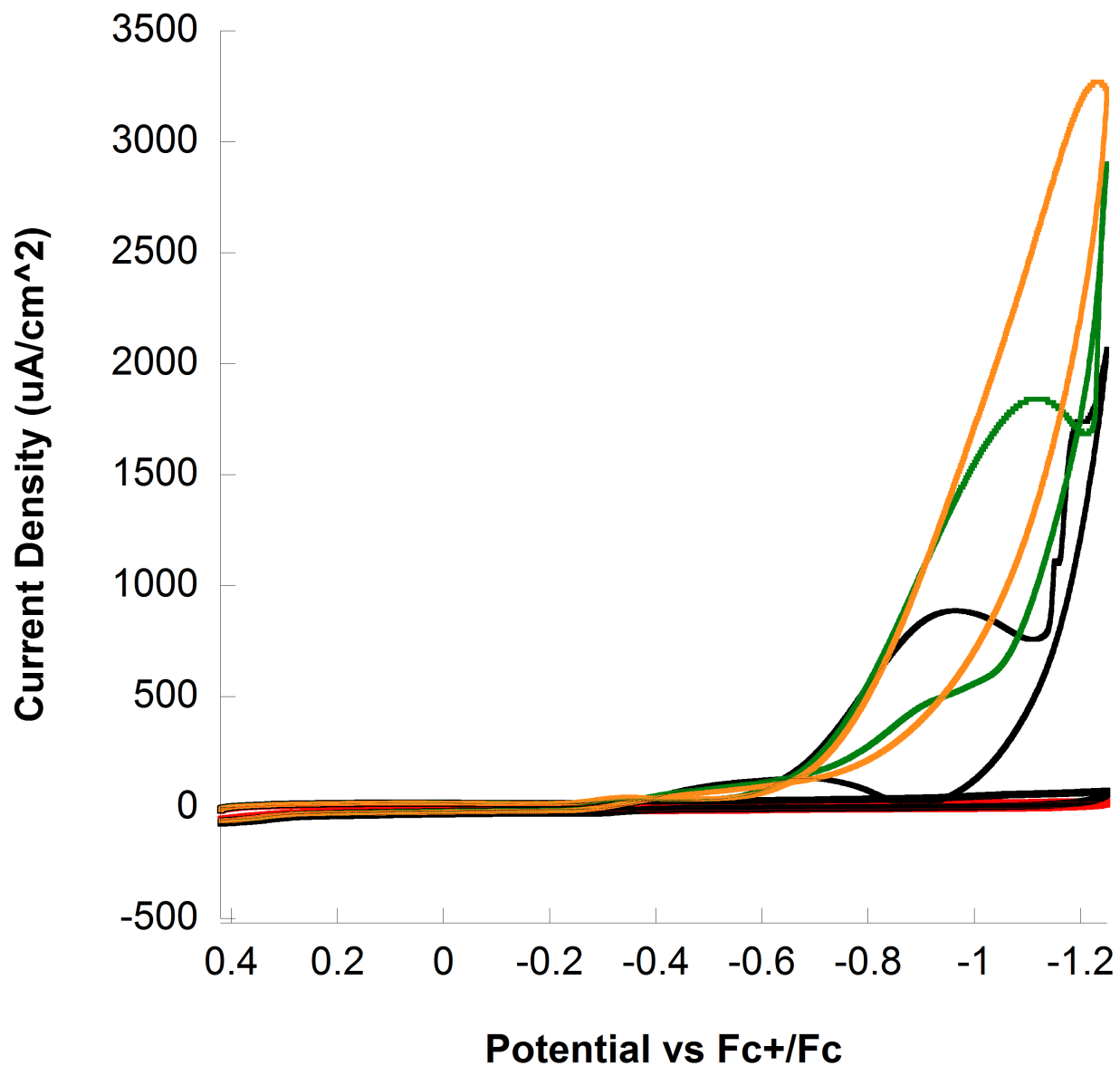


**Figure B5.** CV of **5** in MeCN with 0.1 M TBAPF<sub>6</sub>. Scans were with 0 mM HDMFOTf/Ar (blue), 3.5 mM HDMFOTf/Ar (black), 3.5 mM HDMFOTf/O<sub>2</sub> (black), 7 mM HDMFOTf/O<sub>2</sub> (green), 10.5 mM HDMFOTf/O<sub>2</sub> (orange). All gasses were at 1 atm.



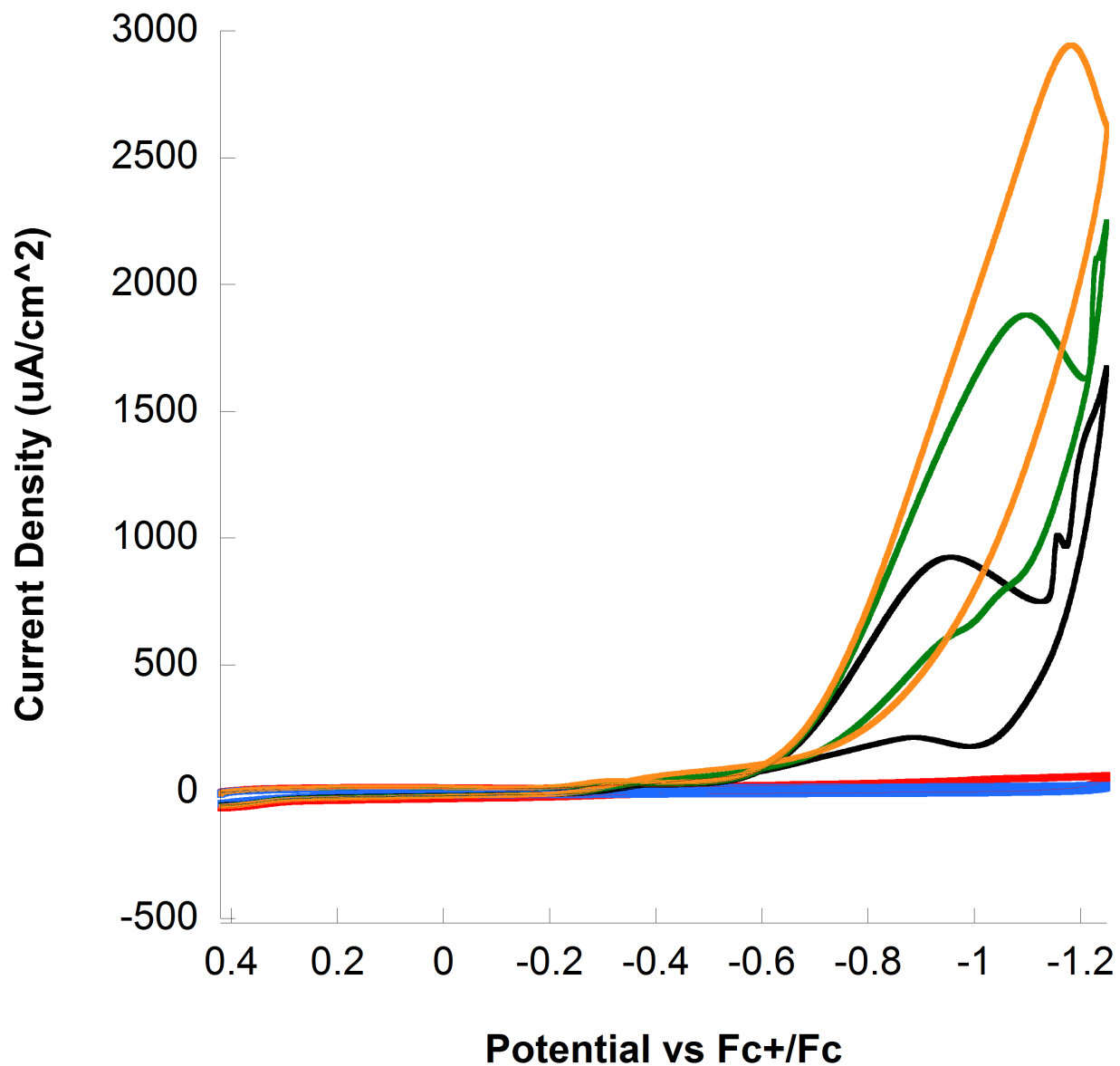


**Figure B6.** CV of 6 in MeCN with 0.1 M TBAPF<sub>6</sub>. Scans were with 0 mM HDMFOTf/Ar (red), 3.5 mM HDMFOTf/Ar (blue), 3.5 mM HDMFOTf/O<sub>2</sub> (black), 7 mM HDMFOTf/O<sub>2</sub> (green), 10.5 mM HDMFOTf/O<sub>2</sub>(orange). All gasses were at 1 atm.

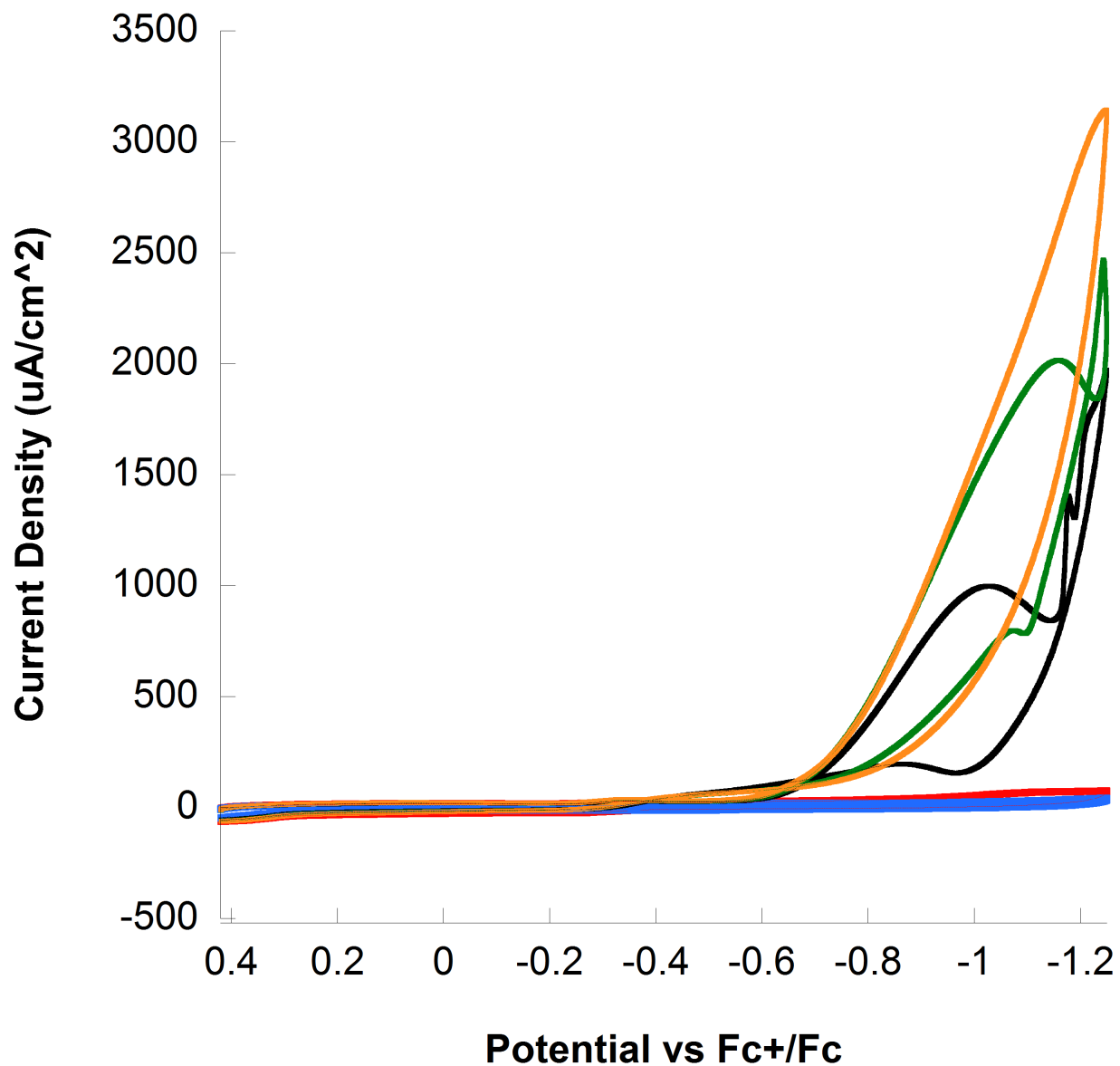


**Figure B7.** CV of 7 in MeCN with 0.1 M TBAPF<sub>6</sub>. Scans were with 0 mM HDMFOTf/Ar (red), 3.5 mM HDMFOTf/Ar (blue), 3.5 mM HDMFOTf/O<sub>2</sub> (black), 7 mM HDMFOTf/O<sub>2</sub> (green), 10.5 mM HDMFOTf/O<sub>2</sub> (orange). All gasses were at 1 atm.

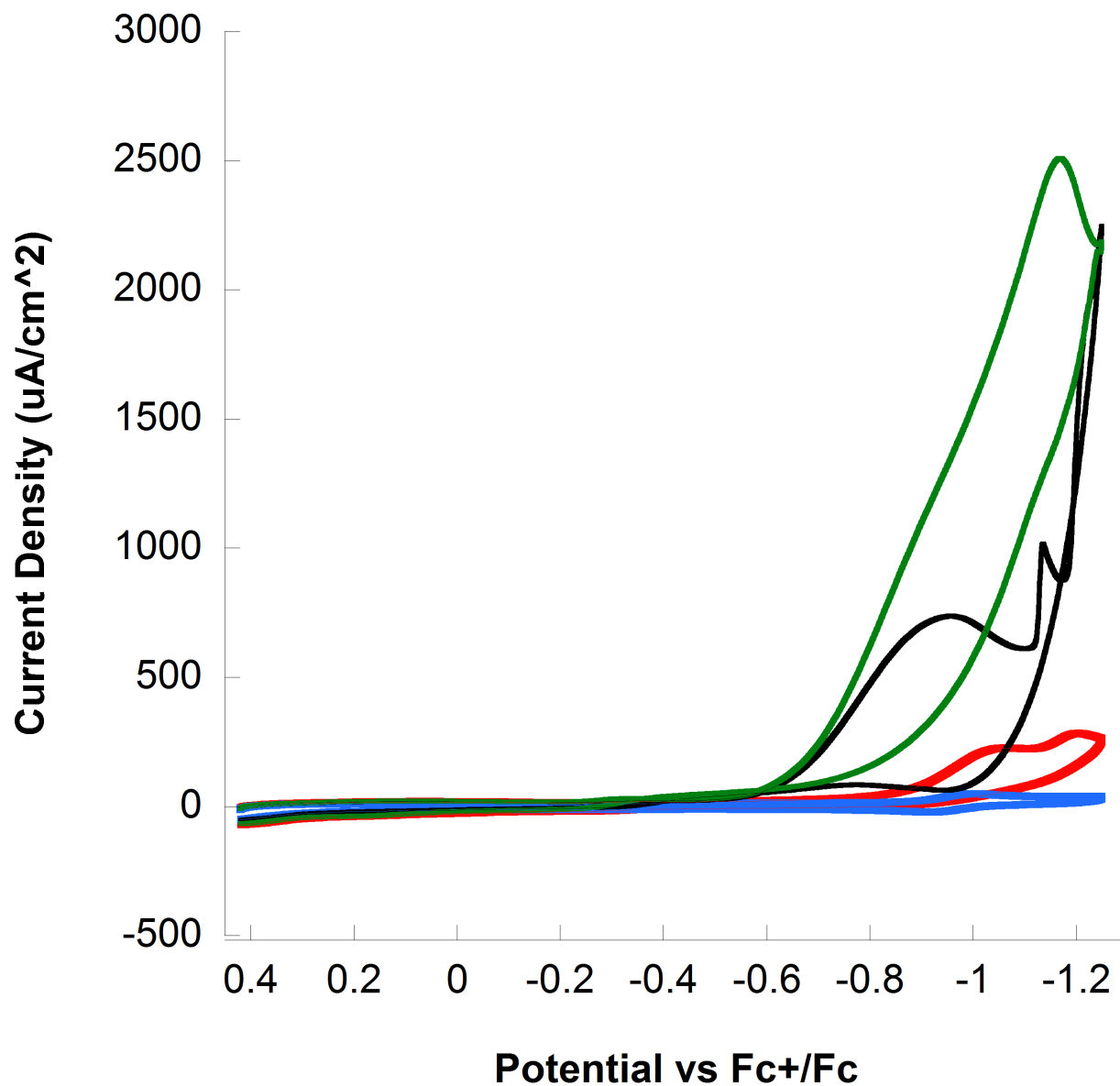


**Figure B8.** CV of **8** in MeCN with 0.1 M TBAPF<sub>6</sub>. Scans were with 0 mM HDMFOTf/Ar (blue), 3.5 mM HDMFOTf/Ar (red), 3.5 mM HDMFOTf/O<sub>2</sub> (black), 10.5 mM HDMFOTf/O<sub>2</sub> (green). All gasses were at 1 atm.

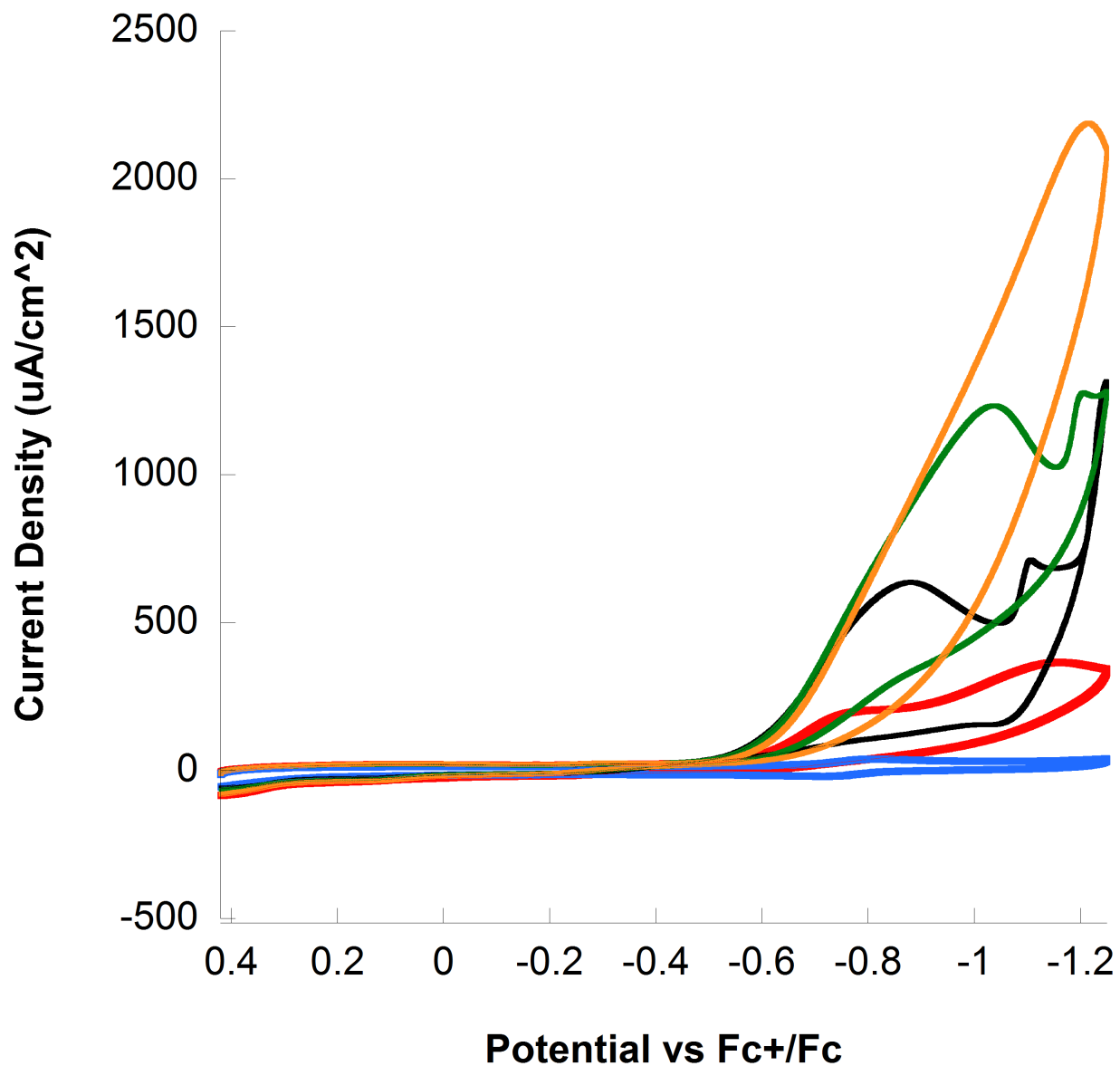


**Figure B9.** CV of 9 in MeCN with 0.1 M TBAPF<sub>6</sub>. Scans were with 0 mM HDMFOTf/Ar (blue), 3.5 mM HDMFOTf/Ar (red), 3.5 mM HDMFOTf/O<sub>2</sub> (black), 7 mM HDMFOTf/O<sub>2</sub> (green), 10.5 mM HDMFOTf/O<sub>2</sub>(orange). All gasses were at 1 atm.

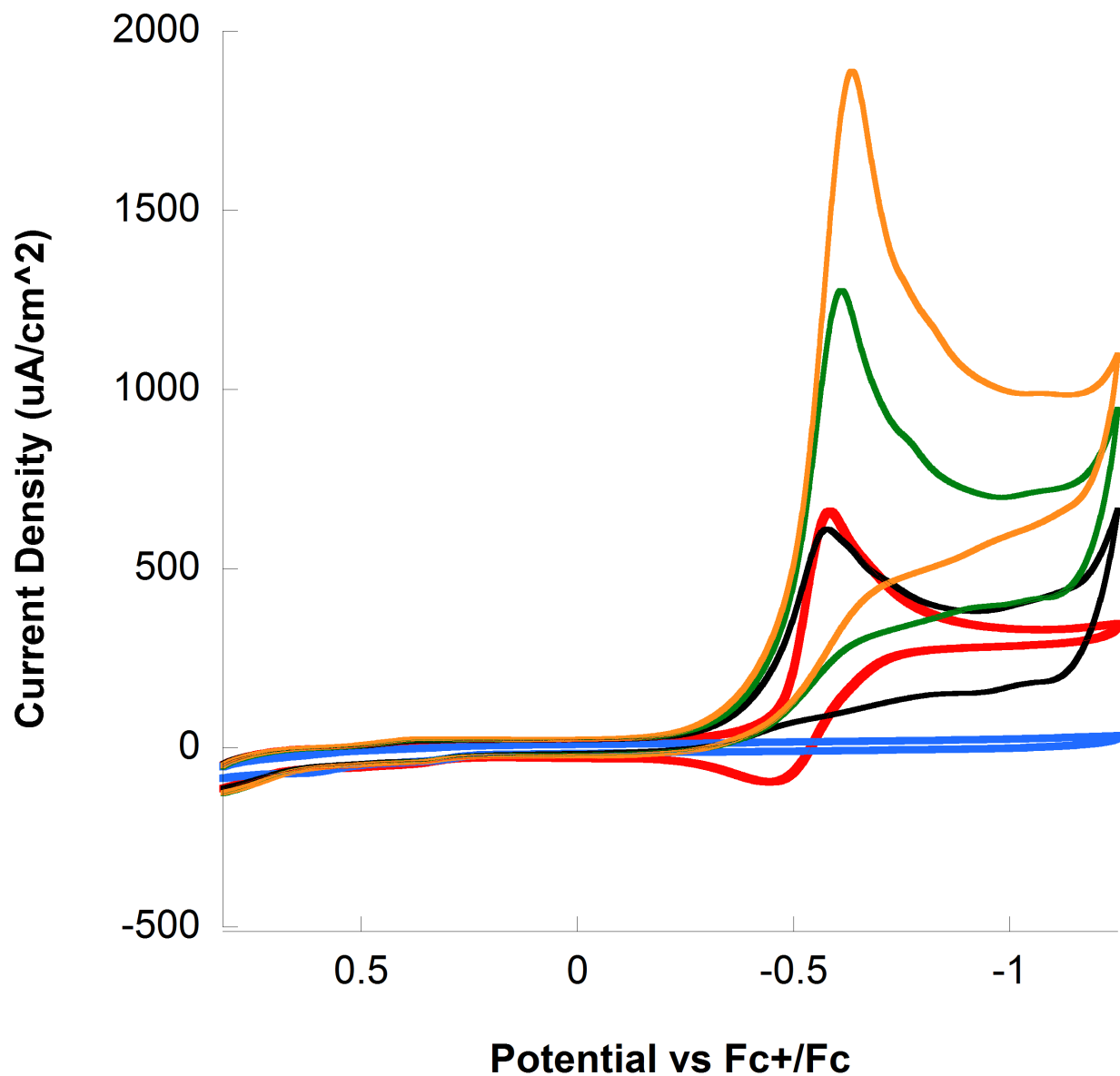


**Figure B10.** CV of **10** in MeCN with 0.1 M TBAPF<sub>6</sub>. Scans were with 0 mM HDMFOTf/Ar (blue), 3.5 mM HDMFOTf/Ar (red), 3.5 mM HDMFOTf/O<sub>2</sub> (black), 7 mM HDMFOTf/O<sub>2</sub> (green), 10.5 mM HDMFOTf/O<sub>2</sub>(orange). All gasses were at 1 atm. This used a Pt working electrode.

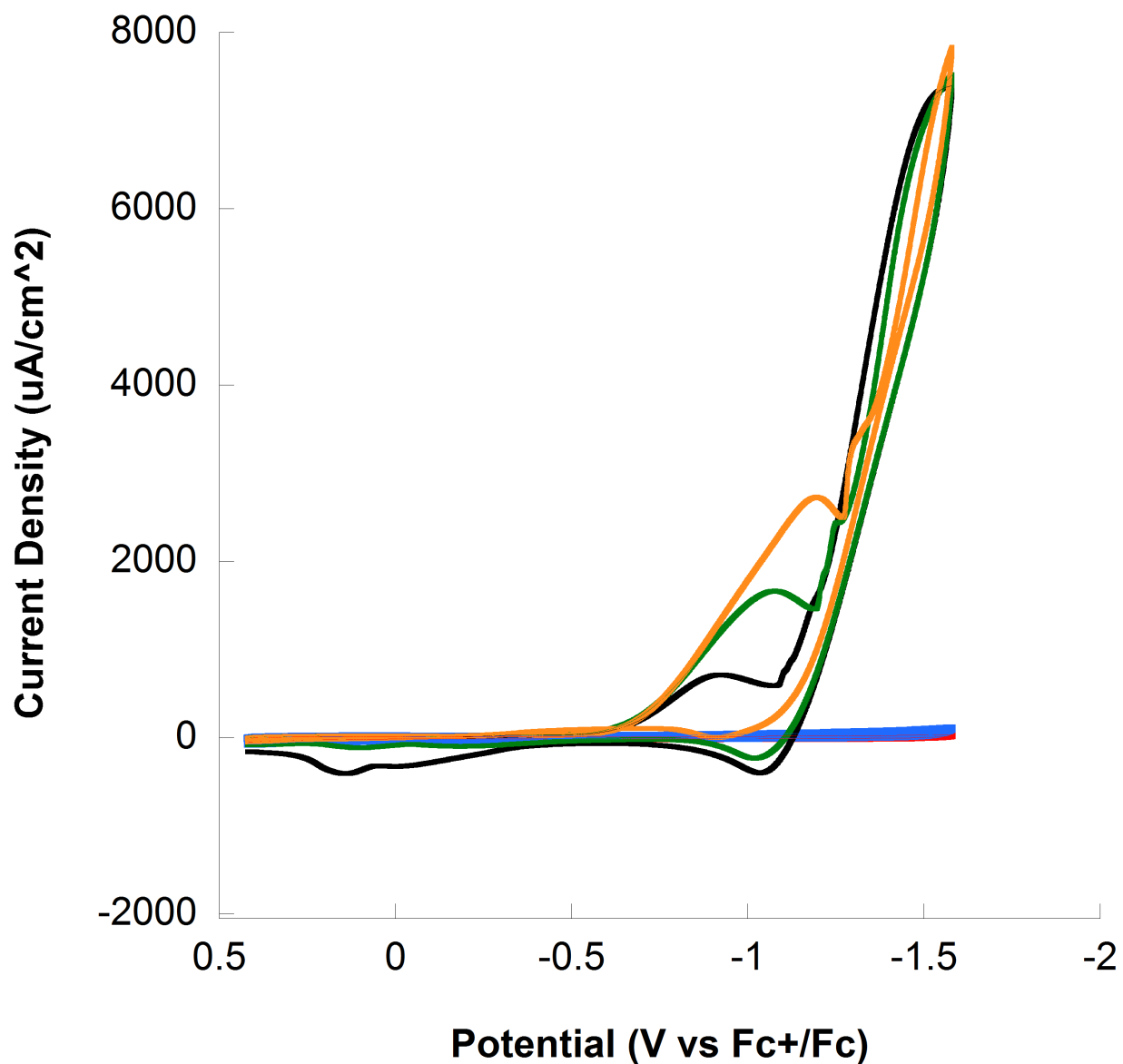


**Figure B11.** Catalyst free CV in MeCN with 0.1 M TBAPF<sub>6</sub>. Scans were with 0 mM HDMFOTf/Ar (blue), 3.5 mM HDMFOTf/Ar (red), 3.5 mM HDMFOTf/O<sub>2</sub> (black), 7 mM HDMFOTf/ O<sub>2</sub> (green), 10.5 mM HDMFOTf/O<sub>2</sub>(orange). All gasses were at 1 atm.

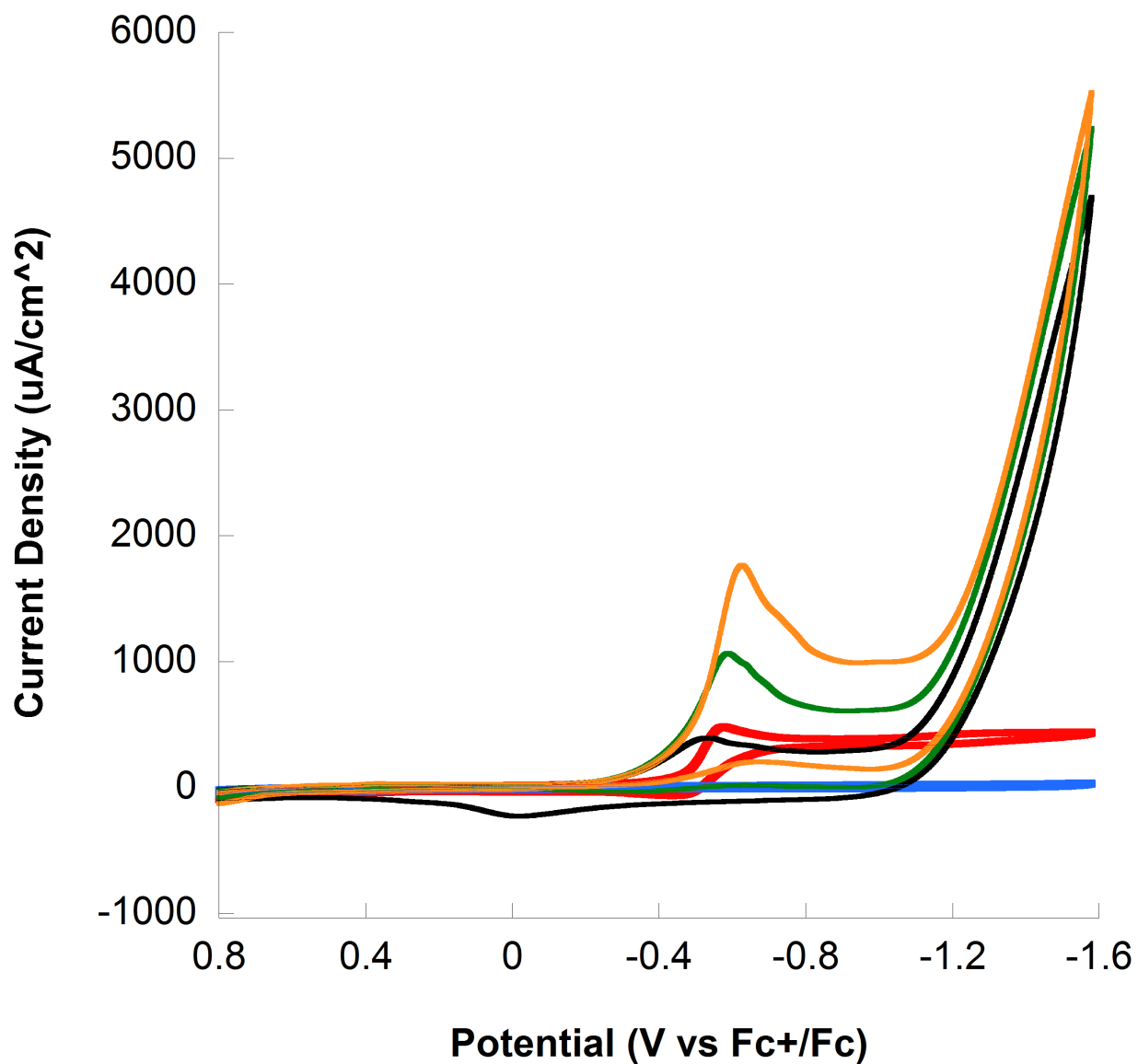


**Figure B12.** Catalyst free CV in MeCN with 0.1 M TBAPF<sub>6</sub>. Scans were with 0 mM HDMFOTf/Ar (blue), 3.5 mM HDMFOTf/Ar (red), 3.5 mM HDMFOTf/O<sub>2</sub> (black), 7 mM HDMFOTf/ O<sub>2</sub> (green), 10.5 mM HDMFOTf/O<sub>2</sub>(orange). All gasses were at 1 atm. This used a Pt working electrode.